Supplementary Information

Trace weak solvation environment enabling ultra-stable high-voltage solid-state lithium metal battery

Ke Yang[1,2], Junyu Jiao[3], Jiabin Ma[1,2], Shizhe Jiao[4], Likun Chen[1,2], Danfeng Zhang[1,2], Yuhang Li[1,2], Xing Cheng[1,2], Jinshuo Mi[1,2], Jie Biao[1,2], Boyu Li[1,2], Xufei An[1,2], Wei Hu[4], Jiaxin Zheng[3], Ming Liu[1*], Feiyu Kang[1,2] and Yan-Bing He[1*]

[1]Shenzhen All-Solid-State Lithium Battery Electrolyte Engineering Research Center, Institute of Materials Research (IMR), Tsinghua Shenzhen International Graduate School, Shenzhen 518055, China.

[2]School of Materials Science and Engineering, Tsinghua University, Beijing 100084, China.

[3]School of Advanced Materials, Peking University, Shenzhen, 518055, China.

[4]School of Future Technology, Department of Chemical Physics, and Anhui Center for Applied Mathematics, University of Science and Technology of China, Hefei, 230026, China.

Correspondence to he.yanbing@sz.tsinghua.edu.cn, liuming@sz.tsinghua.edu.cn

Table of Contents

Supplementary Note 1

The RDFs were performed according to the precise ratio between Li salts, residual DMF solvent and PVDF polymer to evaluate the solvation behavior in the PVDF electrolyte. In detail, a short PVDF chain of -[CH_2-CF_2]$_{10}$- model was built. The molar ratio of LiFSI/DMF/PVDF is 1.427/2.28/0.625.

Supplementary Note 2

When LiFSI (T_m > 200 °C) and TFA (T_m = 72.5 °C) are mixed with an appropriate molar ratio range (1:6 ~ 1:1.8), a homogeneous liquid solution can be obtained. The deep eutectic effect is attributed to complex interactions between TFA and LiFSI. The presence of the functional groups (C=O and NH_2 group) of TFA enables the coordination with cations and anions of LiFSI, respectively. There is a strong interaction between the NH_2 group in TFA and the SO_2 group in LiFSI. These interactions weaken the Coulombic interactions between the FSI^- and Li^+ and induce the breaking of the hydrogen bonds between TFA molecules. The changes of interactions inside the solution could be analyzed by FTIR spectra using the vibration modes of different functional groups. In detail, with increasing the salt concentration, the C=O···Li^+ and -NH_2···SO_2 interactions get stronger, leading to red shift of C=O and N-H vibration modes (Supplementary Fig. 7a, b). Meanwhile, the intramolecular (N−H···O) hydrogen bond between TFA is weakened as evidenced by the gradually weaker peak intensity of N-H vibration mode with increasing the salt concentration. In addition, the -CF_3 group can also coordinate with Li^+, which results in a red shift of the -CF_3 vibration mode in the Raman spectra (Supplementary Fig. 7c).

Supplementary Note 3

The Li-conducting filler $Li_{1.4}Al_{0.4}Ti_{1.6}(PO_4)_3$ nanowires (LNs) were prepared via electrospinning method and annealing process. The SEM image of Supplementary Fig. 16 shows that the LNs consisting of continuous nanoparticles with diameter about 100~130 nm. The XRD peaks suggest that

the crystalline structure of tetragonal phase matches well with the standard pattern of $Li_{1+x}Al_xTi_{2-x}(PO_4)_3$ (LATP) electrolyte. The surface SEM image and energy dispersive spectroscopy (EDS) mapping show that the LNs are uniformly dispersed in the pores between PVDF spherulites to form an interconnecting structure (Supplementary Fig. 17), which contributes to achieve uniform ion flux across the electrolyte and suppress short circuit of batteries, as evidenced by our previous work[24]. The structures of LNs can be well maintained after compositing with PVDF electrolyte. The crystallinity degree and morphology of PVDF remains unchanged for PVLN and PDTL electrolyte (Supplementary Fig. 18-19). These results indicate that the addition of LNs and the replacement of DMF with TFA doesn't affect the morphology and structure of the PVDF electrolyte.

Supplementary Note 4

Due to the deep eutectic effect, we cannot obtain an electrolyte using the single TFA solvent through the solution cast method, because the Li-TFA solution is not enough to dissolve the PVDF powders. Therefore, the TFA acts as co-solvent to partially replace the DMF in the PDTL electrolyte. To maximize the TFA content for the generation of abundant CIPs and AGGs, we prepared several solutions with different TFA/DMF molar ratios (7:3, 6:4, 5:5, 4:6, 3:7) while the Li salts content remains same. As shown in Supplementary Fig. 19a, undissolved LiFSI can be observed when the TFA content > 50 mol% due to its relative weak Li^+ binding energy. Therefore, the maximized content was regulated to be 50 mol% in this work. In a typical experiment, 400 mg TFA was added to 15 mL DMF before the solution cast process to ensure the 50 mol% TFA in the obtained electrolyte.

Supplementary Note 5

We also explored that whether the TFA can change the local high concentrated state in PVDF electrolyte. We prepared an electrolyte film using DMF-TFA co-solvent. The AFM-nano-IR was

applied to detect the C=O group of solvent. A shown in Supplementary Fig. 21, DMF and TFA solvent is also aggregated inside the bulk of the PVDF spherulites. This result demonstrates that despite the interaction of PVDF with TFA is weaker than that with DMF, the replacement of DMF with TFA doesn't change the local high concentrated state of PVDF electrolyte.

Supplementary Note 6 | Supplementary methods

Materials. $Al(NO_3)_3 \cdot 9H_2O$ (99%) and $Ti(OC_4H_9)_4$ (99.5%) were purchased from Macklin. Polyvinyl pyrrolidone (PVP, Mw=1,300,000), $HCON(CH_3)_2$ (DMF) and $C_2F_3NOH_2$ (TFA) came from Sigma Aldrich. $LiNO_3$ (99%), $C_6H_7O_3P$ (98%), $C_6H_8O_7$ (98%) and (99.9%) were purchased from Aladdin. PVDF (M_w=300,000, kynar 761) came from Arkema. LiFSI (99.99%) was purchased from Tinci Materials Technology Co., Ltd. Liquid electrolyte (1 M $LiPF_6$ in ethylene carbonate (EC), dimethyl carbonate (DMC) and ethyl methyl carbonate (EMC) was obtained from Suzhou Qianmin Chemical Reagent Company.

Fabrication of cells. The cathode was prepared by mixing $LiNi_{0.8}Co_{0.1}Mn_{0.1}O_2$ (NCM811), Super P, PVDF 5130 binder in a weight ratio of 80:10:10 in N-methyl-2-pyrrolidone (NMP, 99.9%, Aladdin), followed by casting the slurry on an Al foil. After drying at 80 ºC for overnight, the cathode was prepared with NCM811 mass loading around 2 mg cm^{-2}. The high mass loading cathode is 1 mAh cm^{-2}. The CR2032 solid-state cells were assembled in an Ar-filled glove box without using any liquid electrolyte or solvent. The CR2032 liquid cells were assembled using celgard 2500 separator and l M $LiPF_6$ in EC/DMC/EMC (1:1:1) organic electrolyte.

Calculations. Quantum chemistry calculations were first performed to optimize molecular geometries of DMF and TFA molecules using the Gaussian 16 package at B3LYP/6-311+G(*d,p*) level of theory. The atomic partial charges on these solvent molecules were computed by fitting to the molecular

151 electrostatic potential at atomic centers with the Møller-Plesset second-order perturbation method and
152 the correlation-consistent polarized valence cc-pVTZ(-f) basis set. The atomistic force field parameters
153 for all ions and molecules were described by AMBER format and were adapted from previous work[1].
154 The cross-interaction parameters between different atom types are obtained from the Lorentz-Berthelot
155 combination rule.

156 Atomistic simulations were performed using GROMACS package with cubic periodic boundary
157 conditions[2]. The equations for the motion of all atoms were integrated using a classic Verlet leapfrog
158 integration algorithm with a time step of 1.0 fs. A cutoff radius of 1.6 nm was set for short-range van
159 der Waals interactions and real-space electrostatic interactions. The particle-mesh Ewald (PME)
160 summation method with an interpolation order of 5 and a Fourier grid spacing of 0.20 nm was
161 employed to handle long range electrostatic interactions in reciprocal space. All simulation systems
162 were first energetically minimized using a steepest descent algorithm, and thereafter annealed
163 gradually from 600 K to room temperature (300 K) within 10 ns. All annealed simulation systems were
164 equilibrated in an isothermal-isobaric (NPT) ensemble for 20 ns of physical time maintained using a
165 Nosé-Hoover thermostat and a Parrinello-Rahman barostat with time coupling constants of 0.4 and 0.2
166 ps, respectively, to control the temperature at 300 K and the pressure at 1 atm. Atomistic simulations
167 were further performed in a canonical ensemble (NVT) for 40 ns, and simulation trajectories were
168 recorded at an interval of 100 fs for further structural and dynamical analysis.

169 The HOMO and LUMO was calculated by the first-principles calculation, which was conducted in
170 Gaussian 16 pgram with Becke's three-parameter hybrid method using the Lee-Yang-Parr correlation
171 functional (B3LYP) at 6-311G++G(*d, p*) level. The structures were obtained using the GaussView6.0
172 software.

Li^+ binding energies were calculated by CP2K code[3,4] with DZVP-MOLOPT-SR-GTH basis set[5]. The Pseudopotentials of Goedecker–Teter–Hutter (GTH) method was used to deal the core electrons[6]. The exchange-correlation functional of BLYP was used[7,8]. The complementary plane wave basis set had a cutoff of 600 Ry.

The absorption energies were calculated using first principles density-functional theory[9], performing on Vienna Ab-initio Simulation Package (VASP) code based on Projector Augmented Wave (PAW) method[10]. The Generalized Gradient Approximation of Perdew-Burke-Ernzerh (GGA-PBE)[11] were chose as the exchange-correlation functional. The atomic optimization was calculated by minimizing the energy with Conjugate gradient (CG) quench using the Hellmann-Feynman forces. The kinetic energy cutoff is set at 400 eV for the plane-wave expansion. A Monkhorst-Pack scheme of 1×3×1 with (PVDF series system) k-point mesh were used for Brillouin zone sampling. The convergence criterions for total energy and force were set at 10^{-5} eV and 10^{-2} eV $Å^{-1}$, respectively.

Supplementary Figures

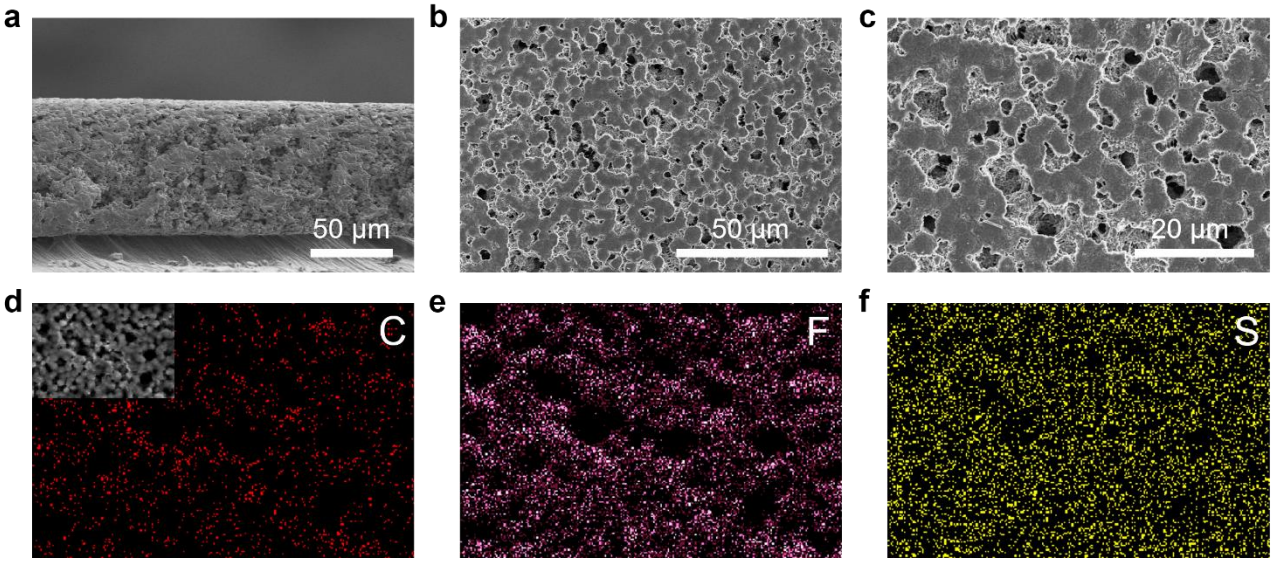

Supplementary Figure 1 | Morphology of PVDF electrolyte. a, Cross-sectional SEM image of PVDF electrolyte. b-f, Surface SEM image of PVDF electrolyte and EDS mapping of C (d), F (e) and S (f) element.

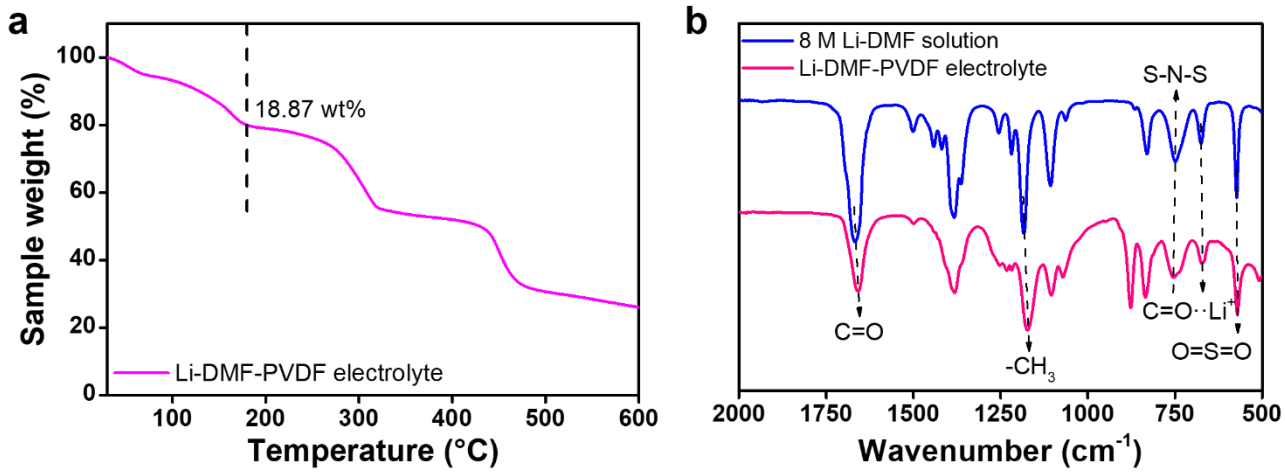

Supplementary Figure 2 | Physicochemical properties of PVDF electrolyte. a, TGA curve of PVDF electrolyte. b, FTIR spectra of 8 M Li-DMF solution and Li-DMF-PVDF electrolyte.

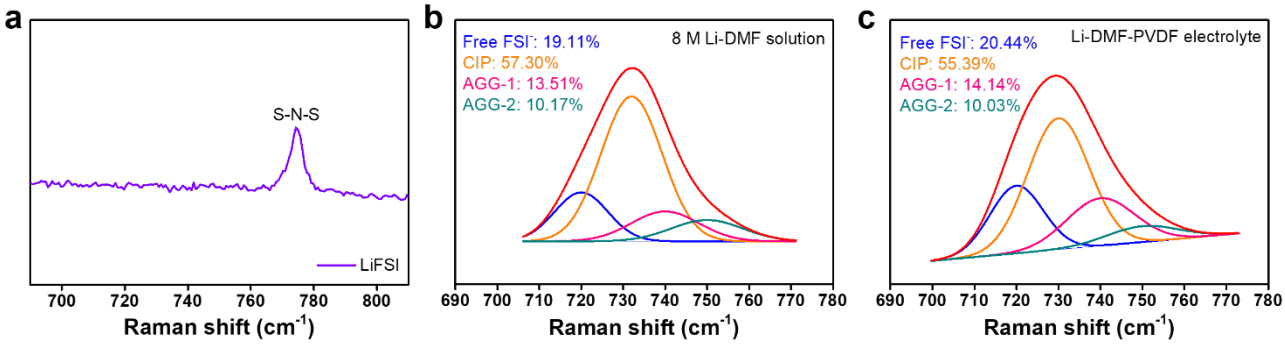

193

194 **Supplementary Figure 3 | Solvation structures analysis of HCLD solution and PVDF electrolyte.**

195 Raman spectra of LiFSI (a), 8 M Li-DMF (b) solution and Li-DMF-PVDF (c) electrolyte.

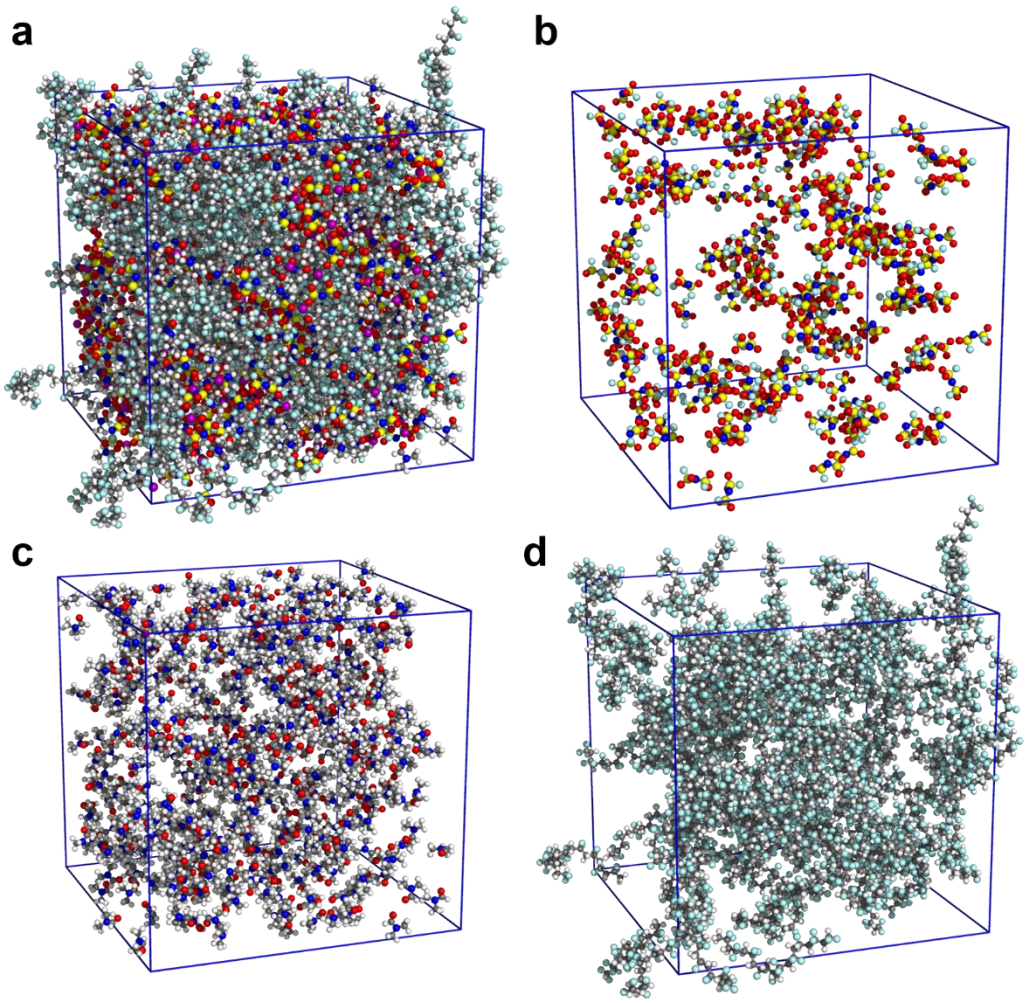

196

197 **Supplementary Figure 4 | MD simulation snapshots of PVDF electrolyte.**

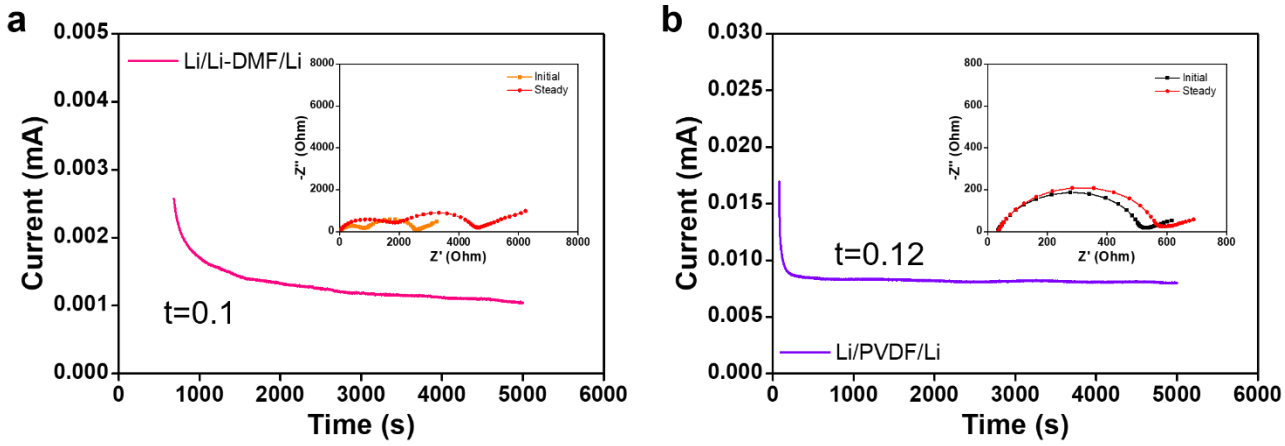

198

199 **Supplementary Figure 5 | Lithium transference number test of HCLD solution and PVDF**
200 **electrolyte.** Chronoamperometry profiles and EIS as well as initial and steady state of the Li||Li
201 symmetric cells using 8 M Li-DMF (a) solution and PVDF (b) electrolyte.

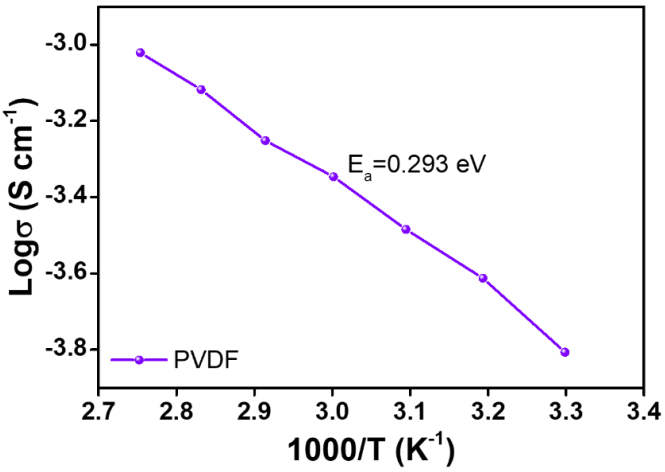

202

203 **Supplementary Figure 6 | Arrhenius plots of ionic conductivities of PVDF electrolyte.**

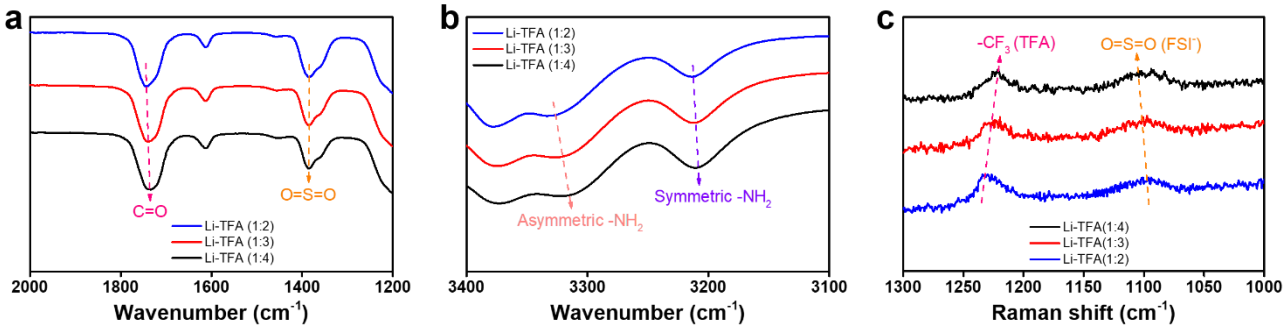

Supplementary Figure 7 | FTIR and Raman spectra of Li-TFA solutions.

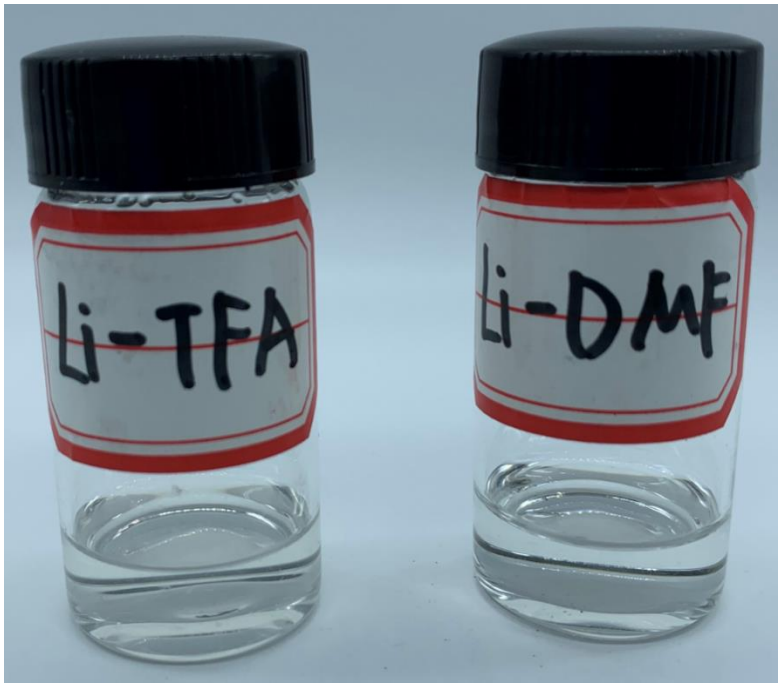

206

207 **Supplementary Figure 8 | Optical photographs of Li-TFA(1:2) and Li-DMF(1:2) solution.**

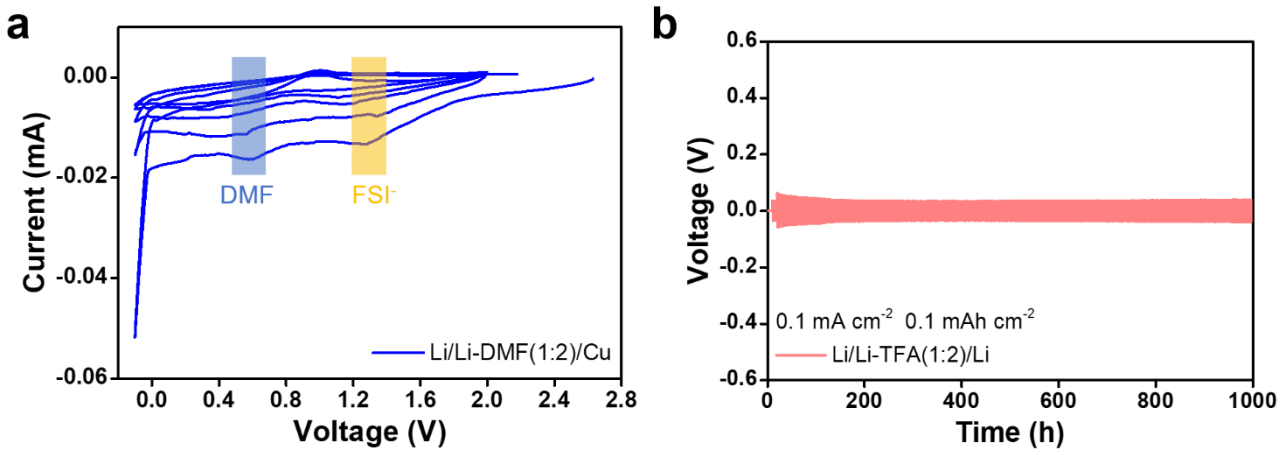

208

209 **Supplementary Figure 9 | Li metal compatibility tests of Li-DMF(1:2) and Li-TFA(1:2) solution.**

210 a, CV curves of Li||Cu cells with Li-DMF(1:2) solution. b, Galvanostatic cycling curves of Li||Li

211 symmetric cells using Li-TFA(1:2) solution.

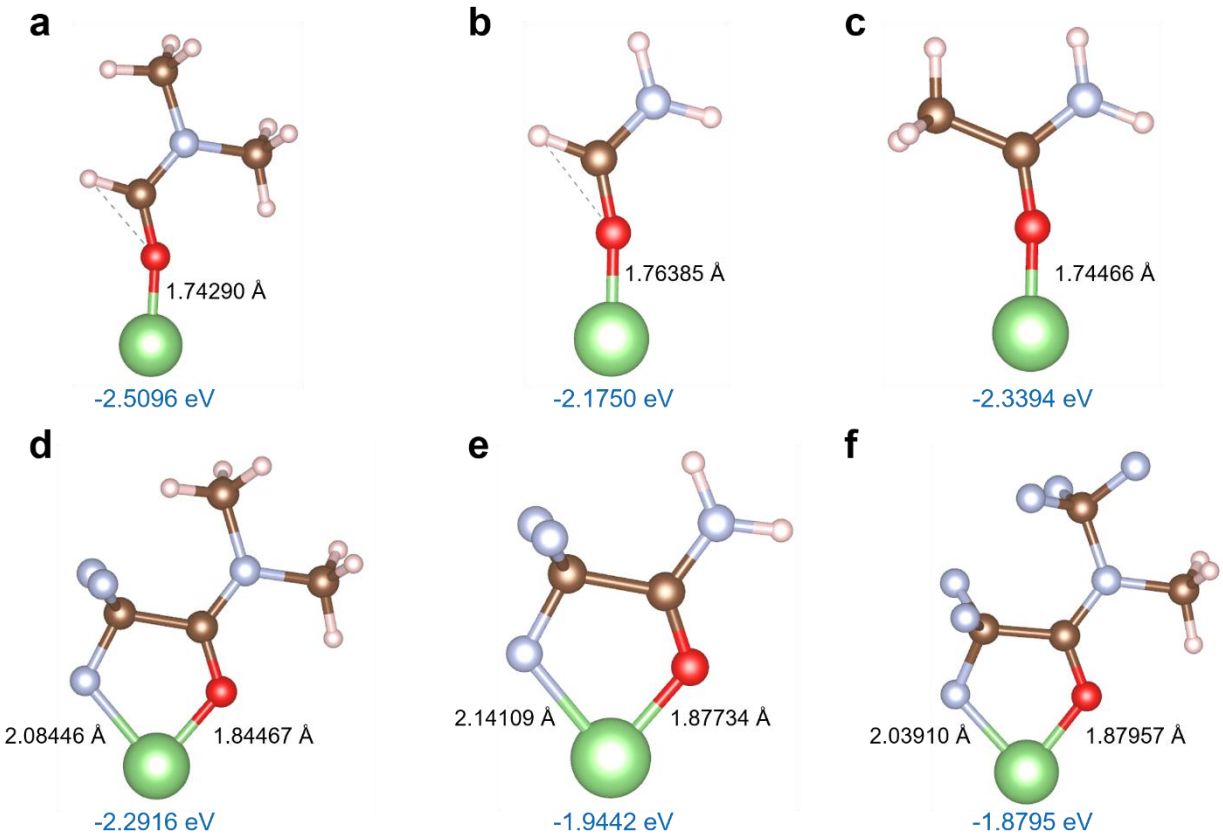

212

213 **Supplementary Figure 10 | Geometries of solvent-Li^+ coordination, binding energies and**

214 **interatomic distances.**

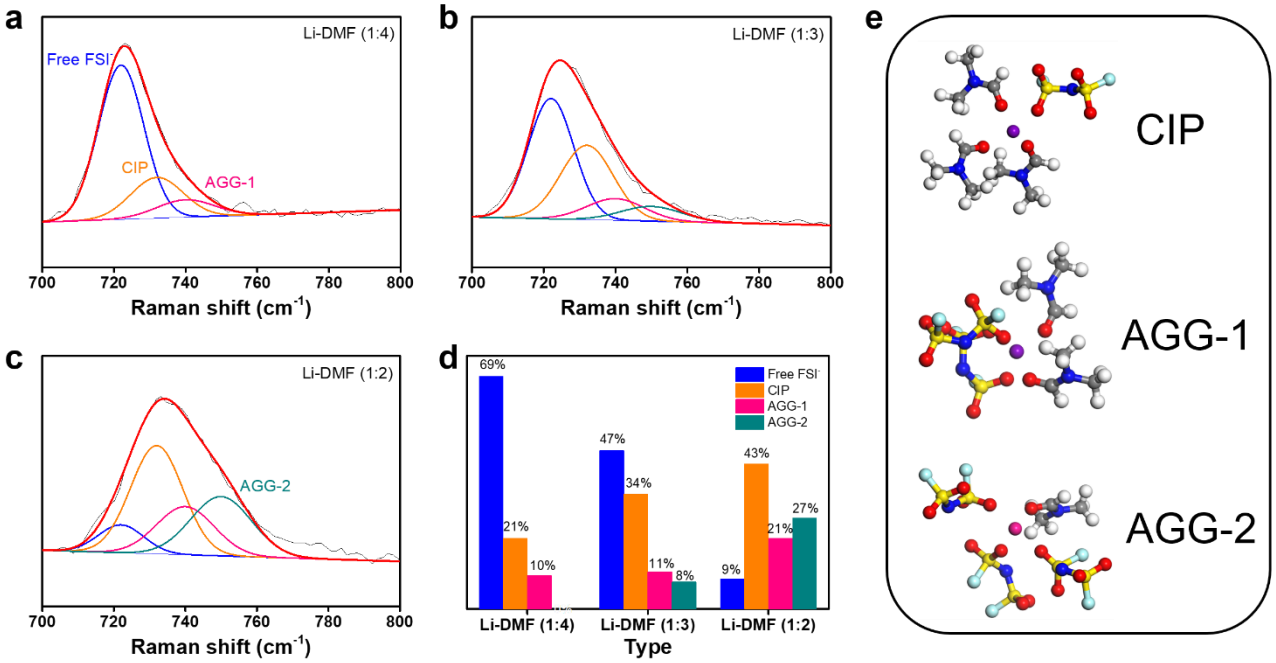

215

216 **Supplementary Figure 11 | Solvation structures analysis of Li-DMF solutions.** Raman spectra of
217 Li-DMF solutions at 1:4 (a), 1:3 (b) and 1:2 (c). d, solvation structures percentages of Li-DMF
218 solutions. e, Schematic illustrations of CIP, AGG-1 and AGG-2.

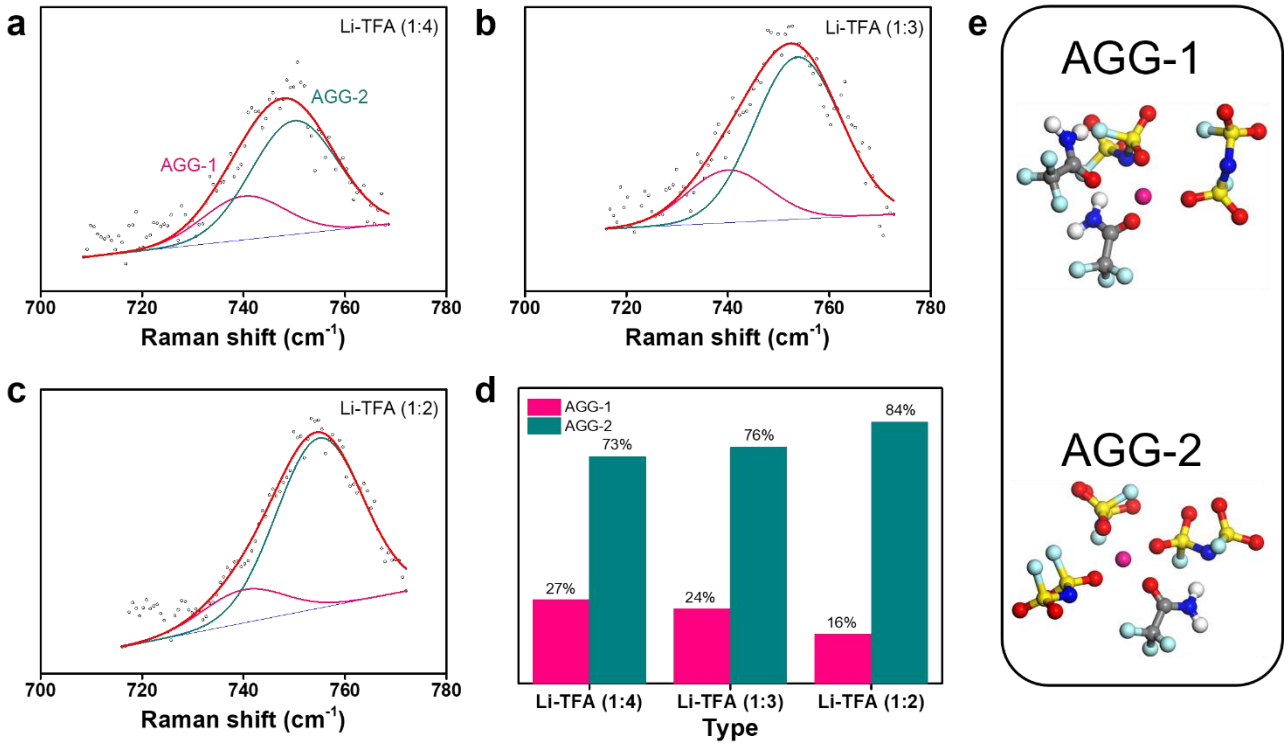

Supplementary Figure 12 | Solvation structures analysis of Li-TFA solutions. Raman spectra of Li-TFA solutions at 1:4 (a), 1:3 (b) and 1:2 (c). d, solvation structures percentages of Li-TFA solutions. e, Schematic illustrations of AGG-1 and AGG-2.

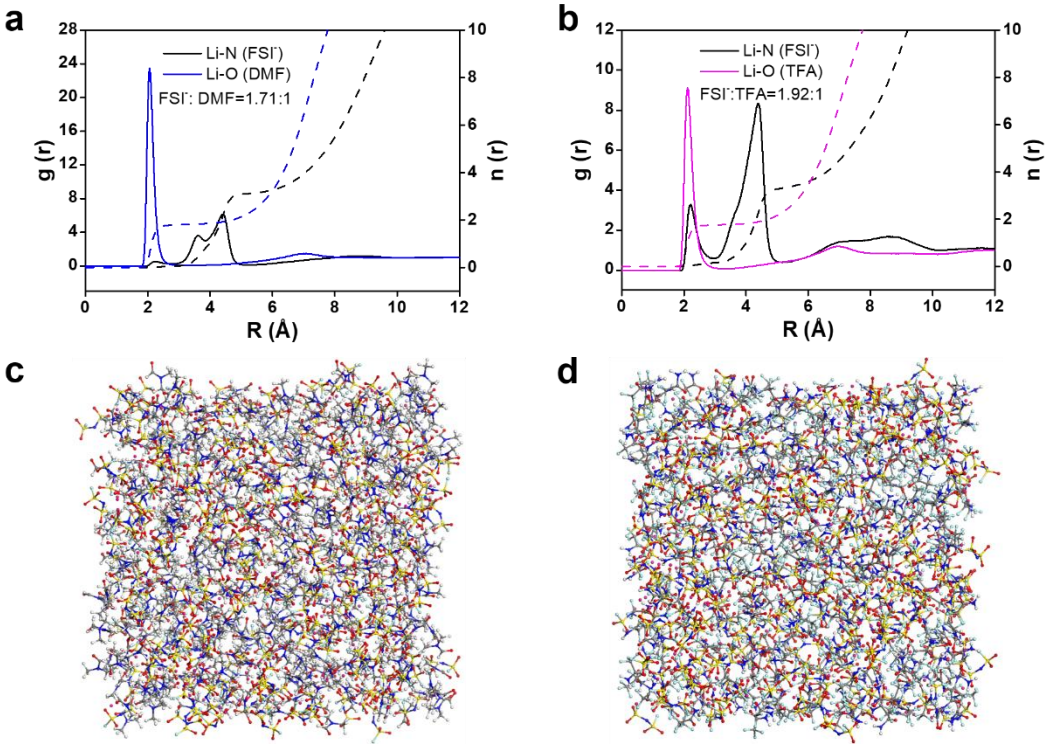

223

224 **Supplementary Figure 13 | Average coordination number calculations.** RDFs and MD simulation

225 snapshots of Li-DMF(1:2) (a, c) and Li-TFA(1:2) (b, d) solution.

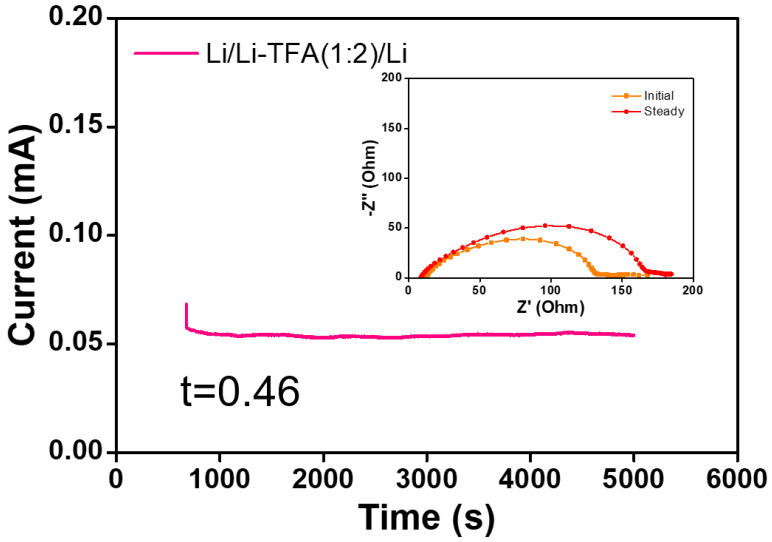

226

227 **Supplementary Figure 14 | Lithium transference number test of Li-TFA(1:2) solution.**
228 Chronoamperometry profiles and EIS as well as initial and steady state of the Li||Li symmetric cells
229 using Li-TFA(1:2) solution.

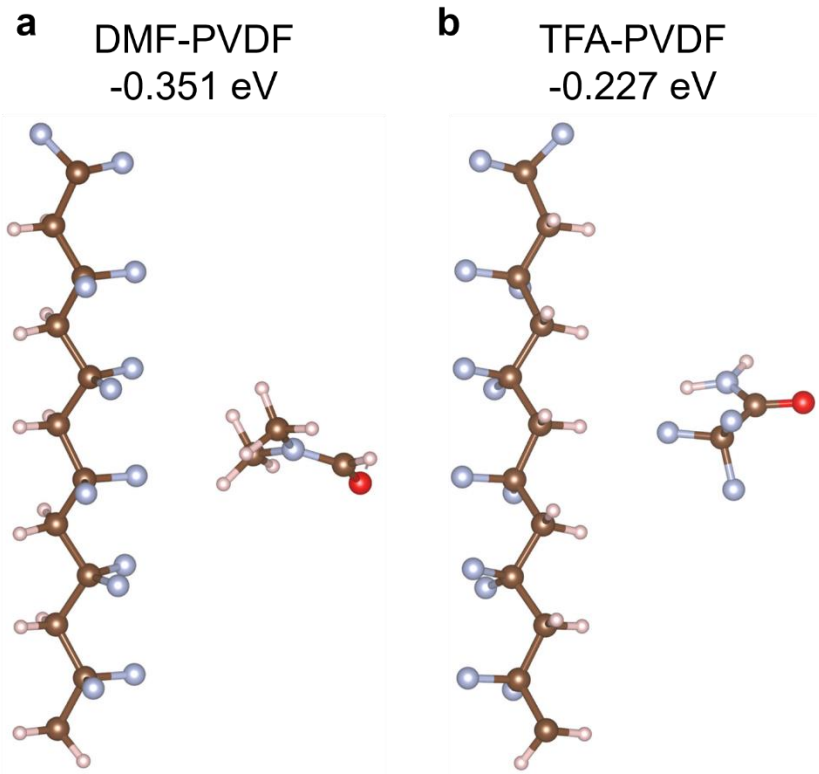

Supplementary Figure 15 | DFT calculation results and geometries of adsorption energies.

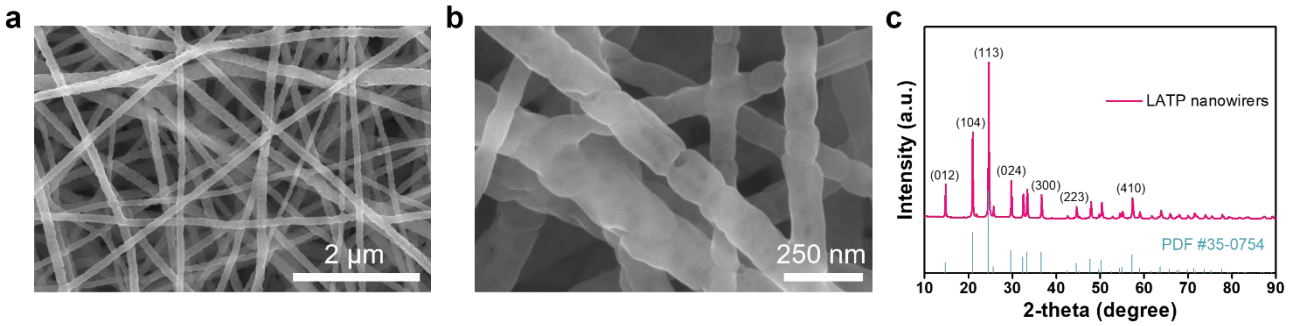

232

233 **Supplementary Figure 16 | Morphology of LNs.** SEM images of LNs at 20000× (a) and 100000×

234 (b). c, XRD pattern of LNs.

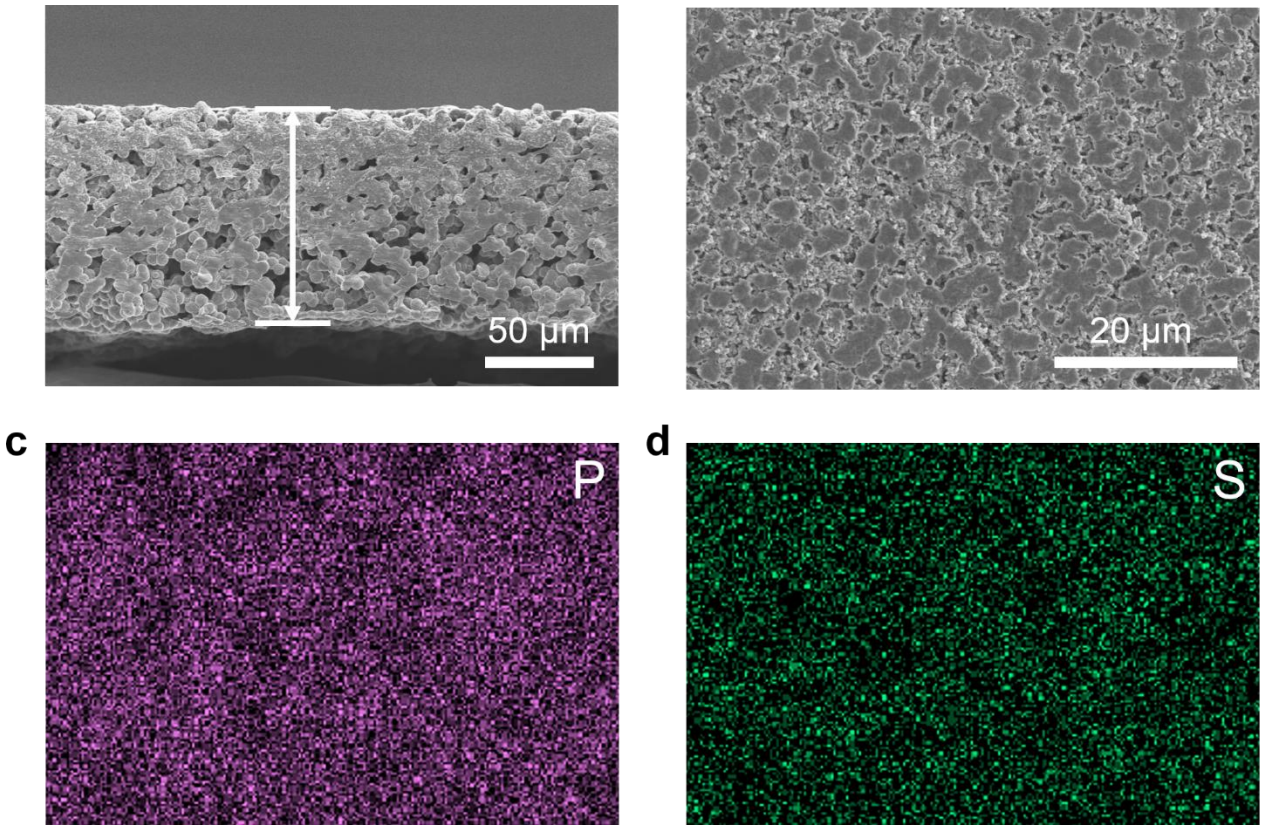

Supplementary Figure 17 | Morphology of PVLN electrolyte. a, Cross-sectional SEM image of PVLN electrolyte. b-d, Surface SEM image of PVLN electrolyte and EDS mapping of P (c) and S (d) element.

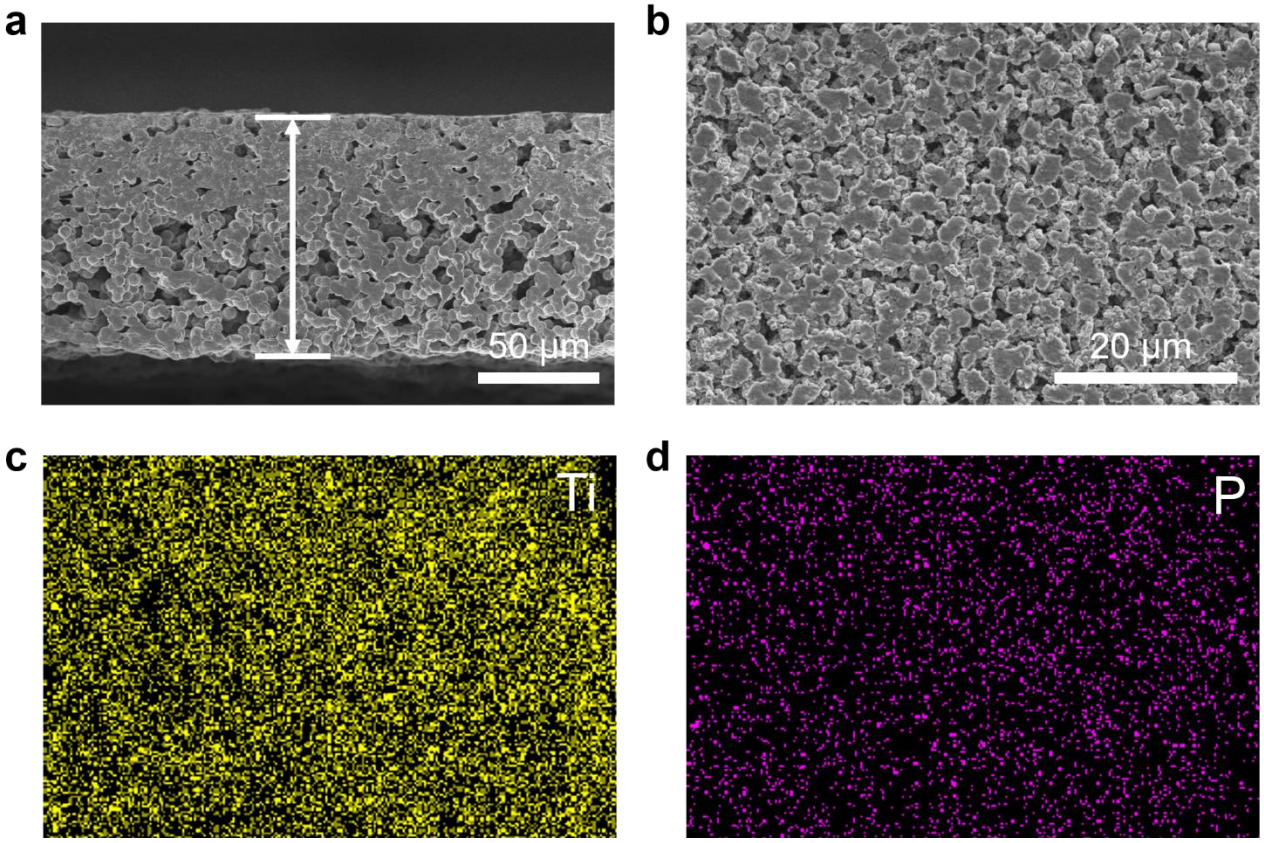

Supplementary Figure 18 | Morphology of PDTL electrolyte. a, Cross-sectional SEM image of PDTL electrolyte. b-d, Surface SEM image of PDTL electrolyte and EDS mapping of Ti (c) and P (d) element.

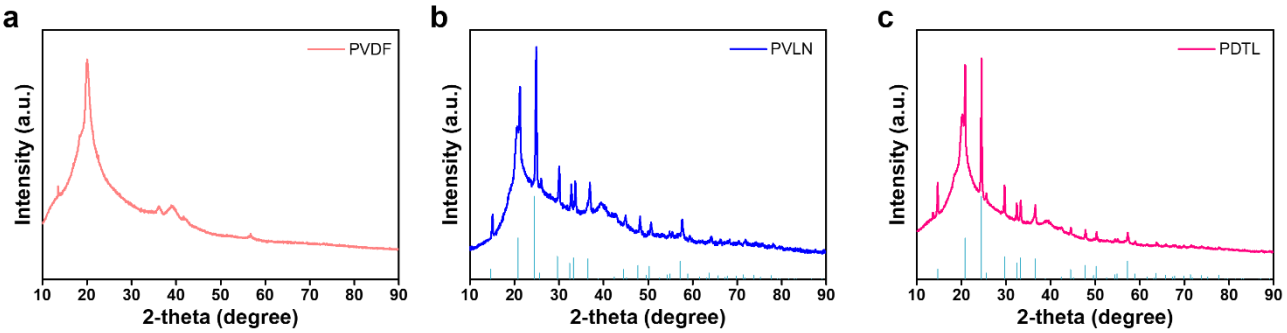

243

244 **Supplementary Figure 19 | Structure characterizations of electrolytes.** XRD patterns of PVDF (a)

245 electrolyte, PVLN (b) electrolyte and PDTL (c) electrolyte.

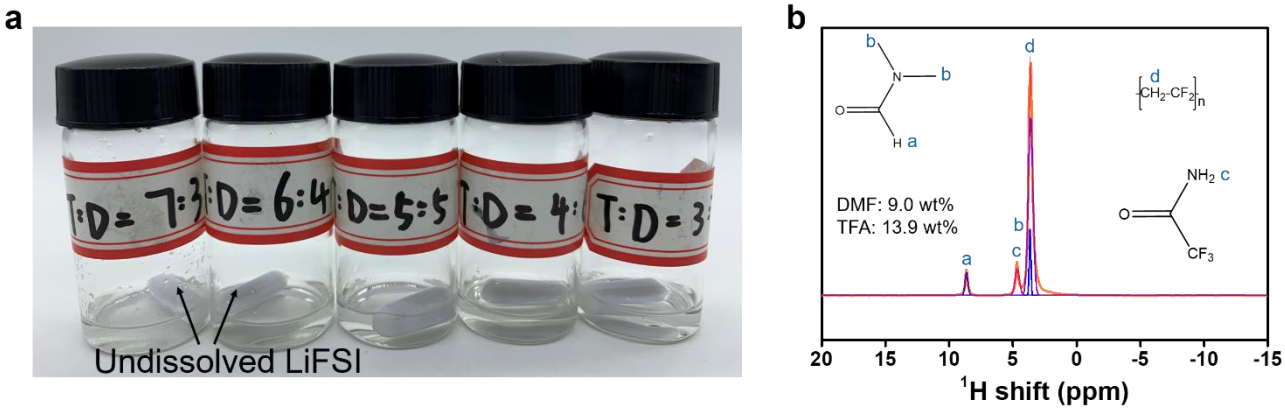

246

247 **Supplementary Figure 20 | Solvent replacement pre-experiments and characterizations.** a,
248 Optical photographs of Li-DMF-TFA solutions at different TFA/DMF ratios. b, ^{1}H solid-state NMR
249 spectra of PDTL electrolyte.

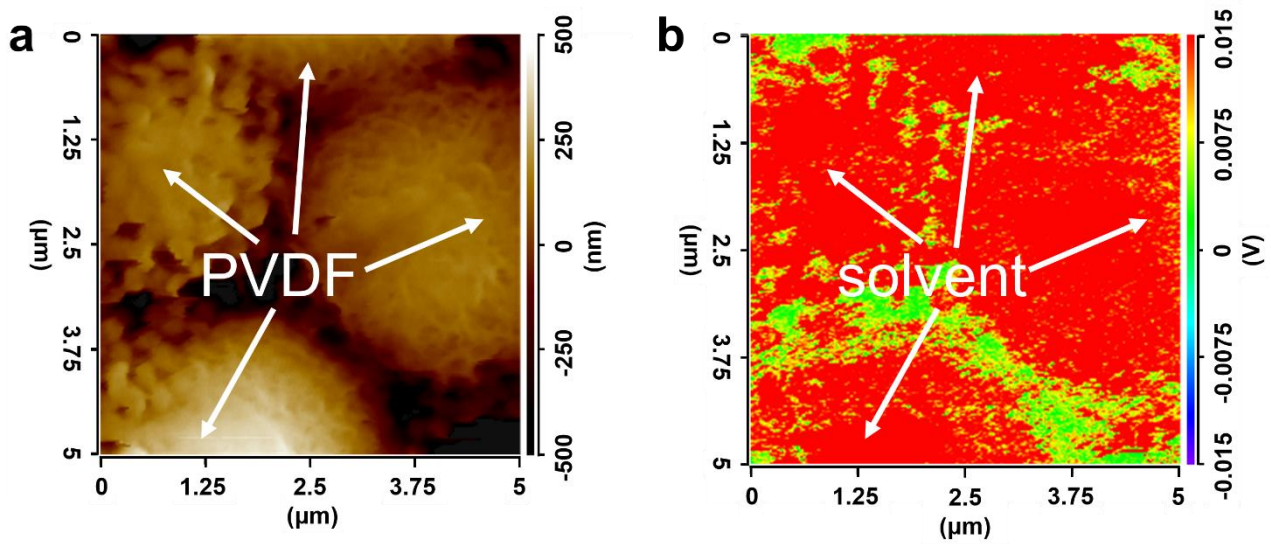

250

251 **Supplementary Figure 21 | AFM image and solvent distribution overlap of PVDF electrolyte**

252 **prepared by DMF-TFA co-solvent.**

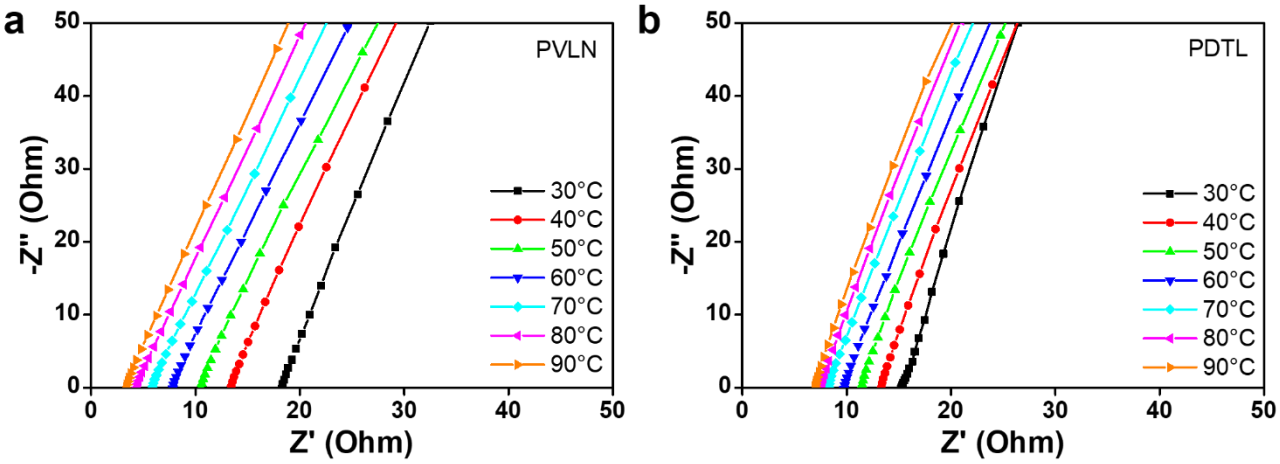

253

254 **Supplementary Figure 22 | Ion transport activation energy tests of electrolytes.** EIS of SS||SS cells

255 at different temperatures of PVLN (a) and PDTL (b) electrolyte.

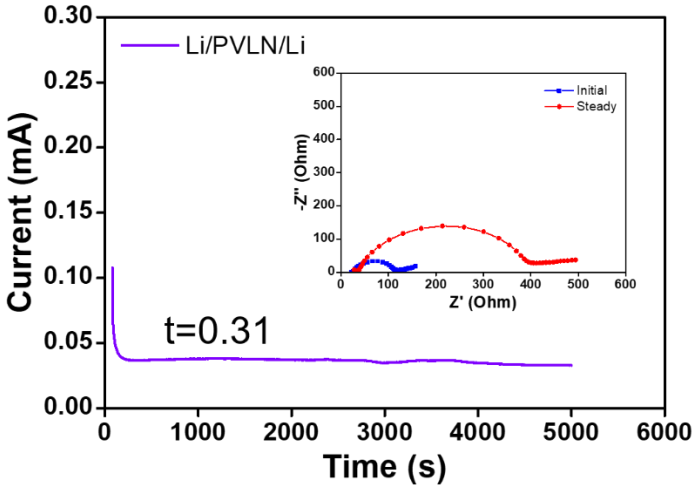

Supplementary Figure 23 | Lithium transference number test of PVLN electrolyte. Chronoamperometry profiles and EIS as well as initial and steady state of the Li||Li symmetric cells using PVLN electrolyte.

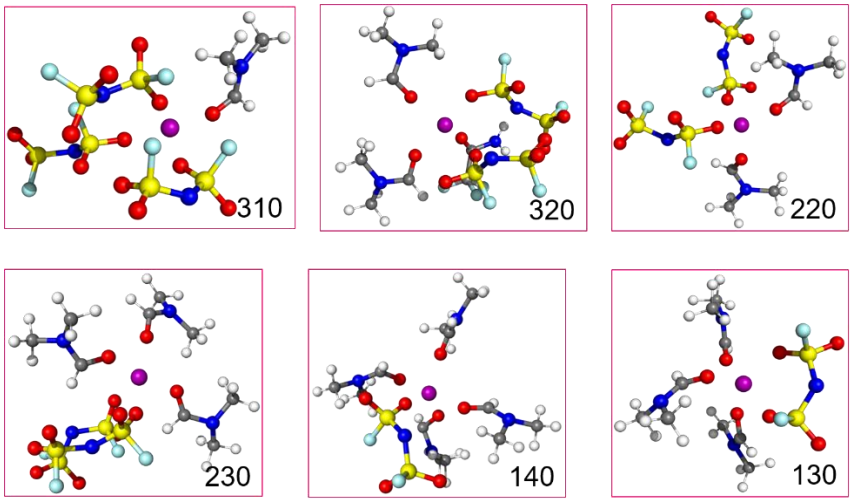

Supplementary Figure 24 | Geometries of solvation structures in PVLN electrolyte.

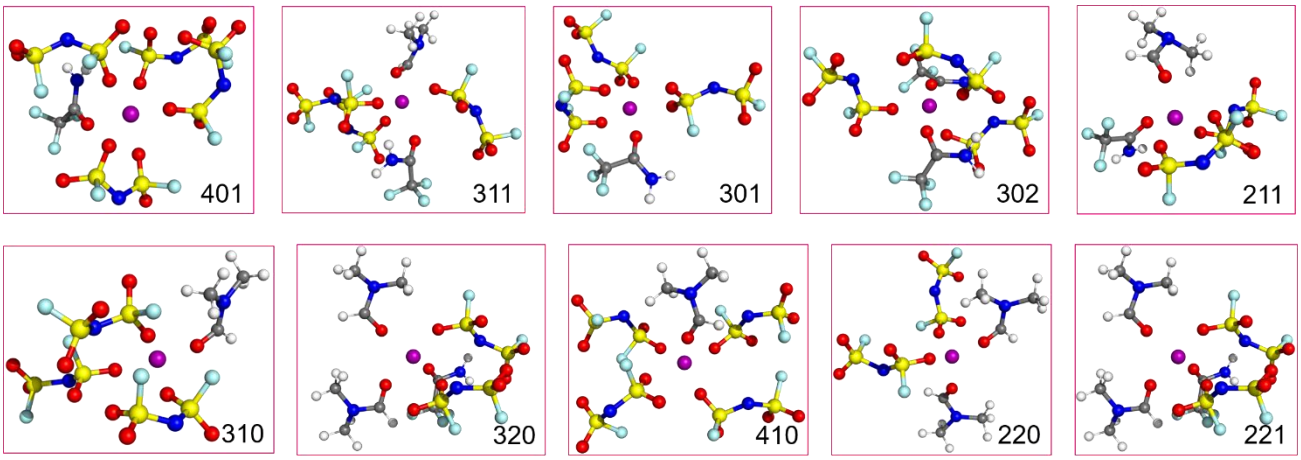

Supplementary Figure 25 | Geometries of solvation structures in PDTL electrolyte.

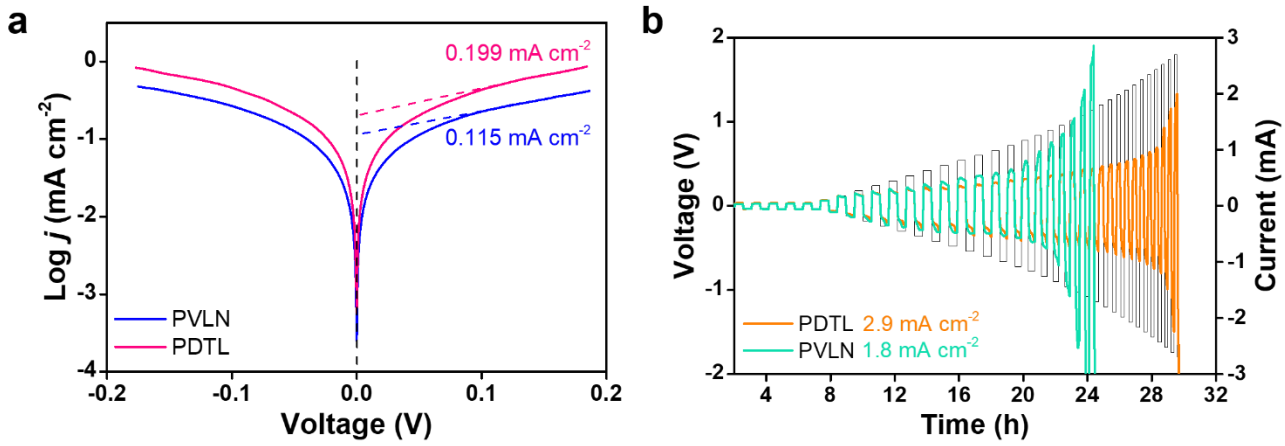

264

265 **Supplementary Figure 26 | Electrochemical characterizations of Li metal compatibility.** a,
266 Exchange current densities of Li||PVLN||Li and Li||PDTL||Li symmetric cells. b, Critical current
267 densities of Li||PVLN||Li and Li||PDTL||Li symmetric cells.

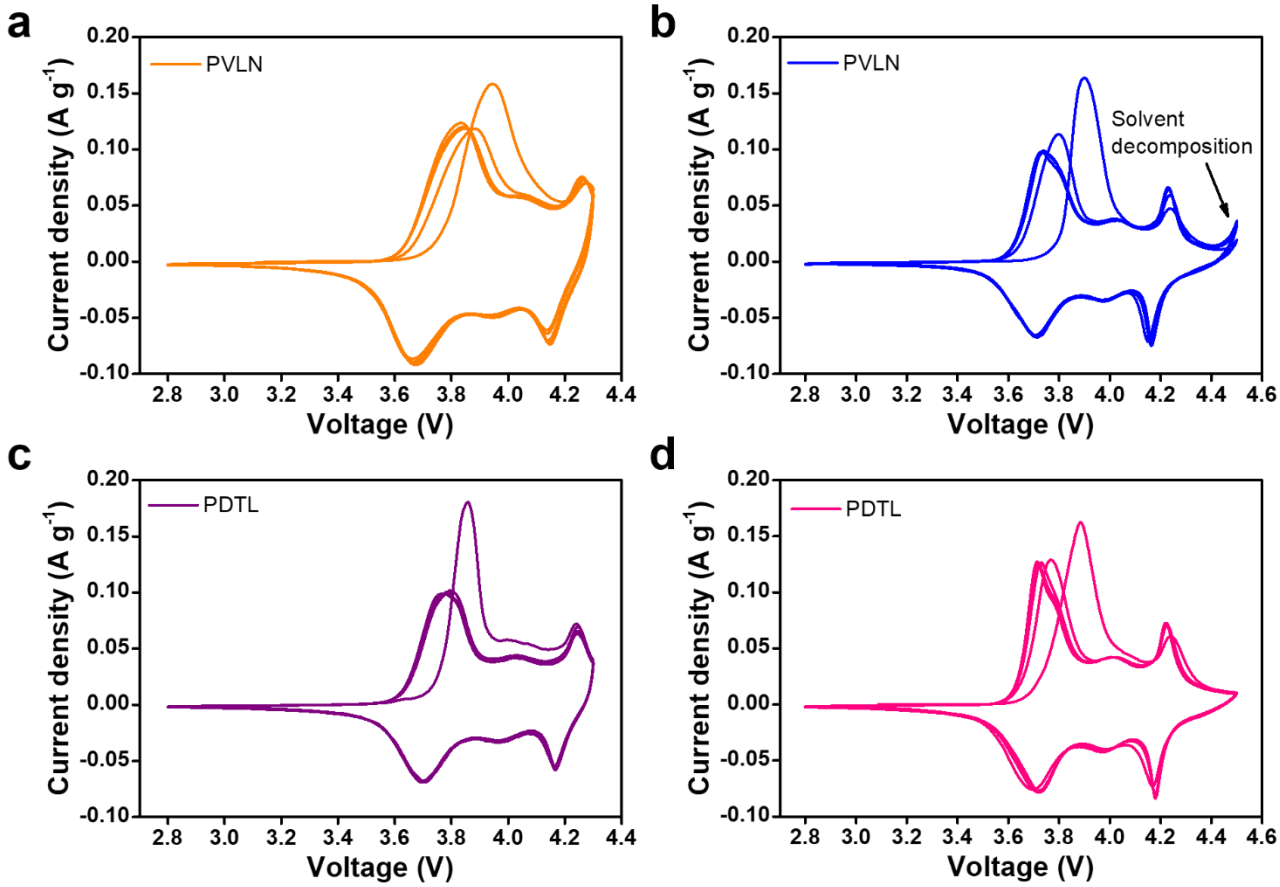

Supplementary Figure 27 | CV curves of Li||NCM811 full cells. CV curves of Li||PVLN||NCM811 (a, b) and Li||PDTL||NCM811 (c, d) full cells.

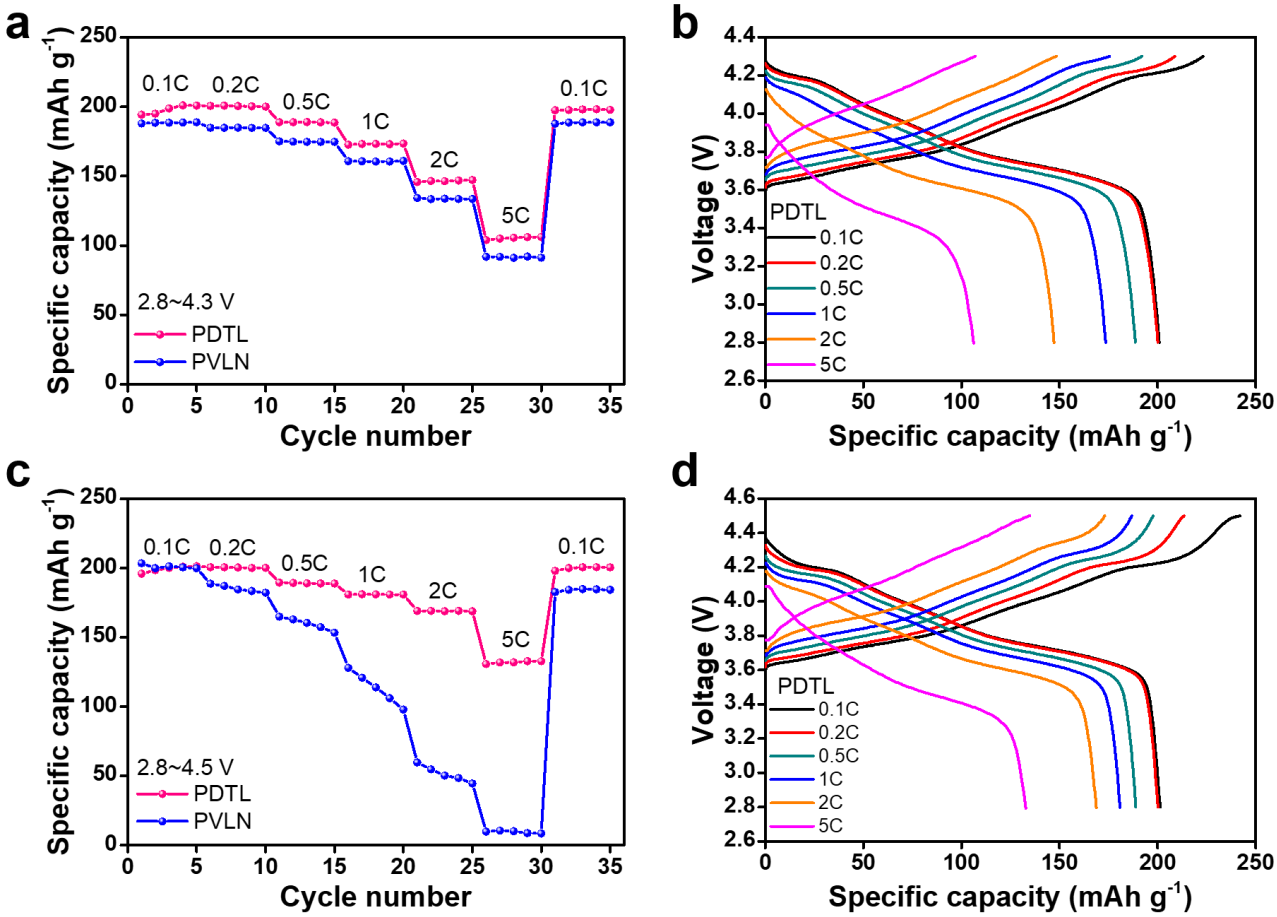

Supplementary Figure 28 | Rate performances of Li||NCM811 full cells. Rate capacities of full cells under 2.8~4.3 V (a) and 2.8~4.5 V (c). Charge/discharge curves at different rates of Li||PDTL||NCM811 cells under 2.8~4.3 V (b) and 2.8~4.5 V (d).

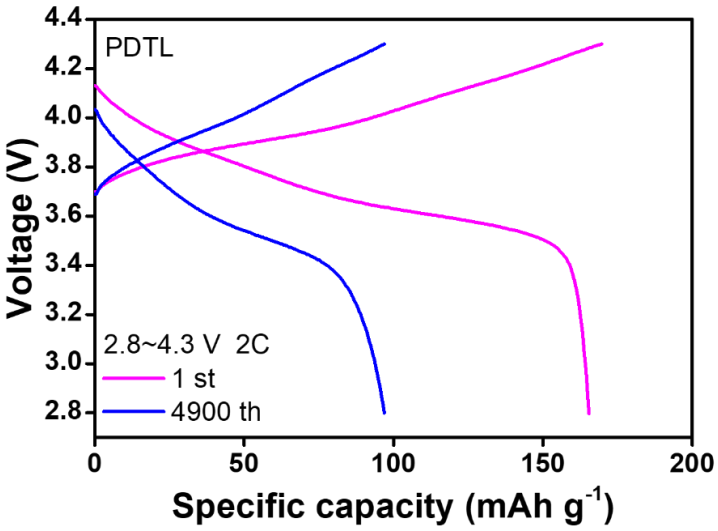

275

276 **Supplementary Figure 29 | Charge/discharge curves of Li||PDTL||NCM811 full cells under**

277 **2.8~4.3 V.**

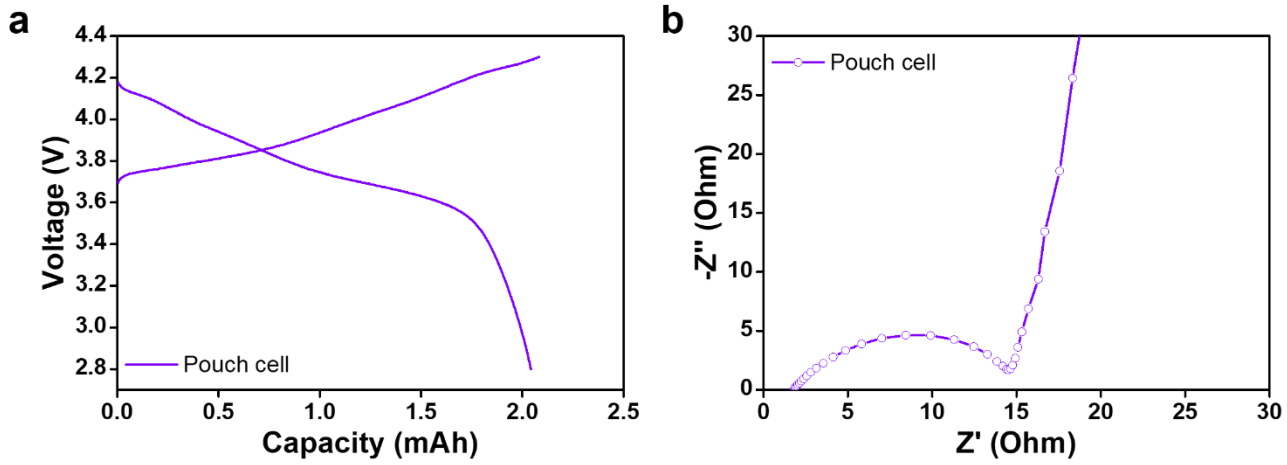

278

279 **Supplementary Figure 30 | Electrochemical performances of Li||NCM811 pouch cell.** a,

280 Charge/discharge curves of pouch cells. b, EIS of pouch cells.

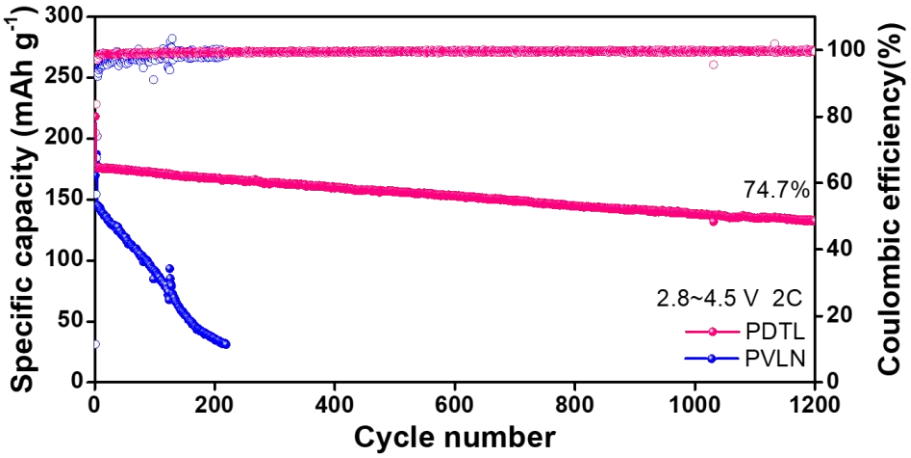

281

282 **Supplementary Figure 31 | Cycling stability of Li||NCM811 full cells at 2.8~4.5 V, 2C.**

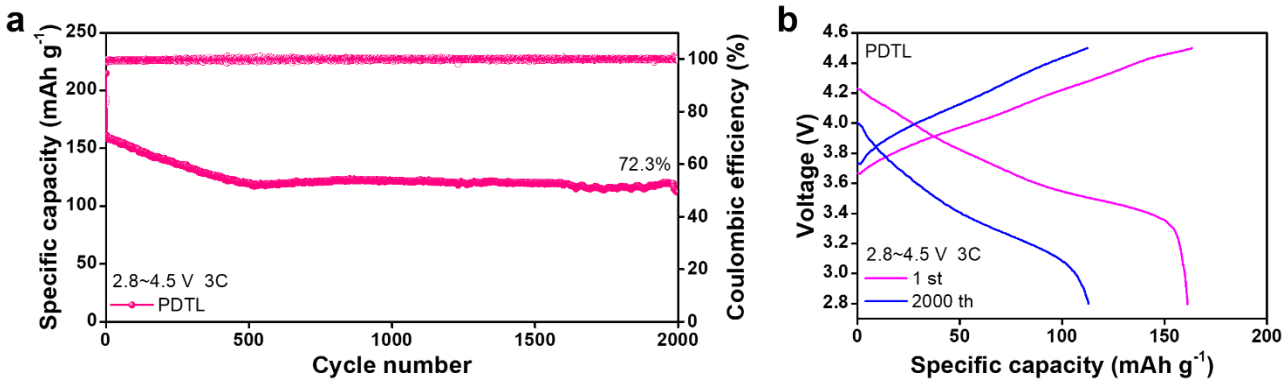

283

284 **Supplementary Figure 32 | Electrochemical performance of Li||PDTL||NCM811 full cells at**

285 **2.8~4.5 V, 3C.** a, cycling stability. b, Charge/discharge curves.

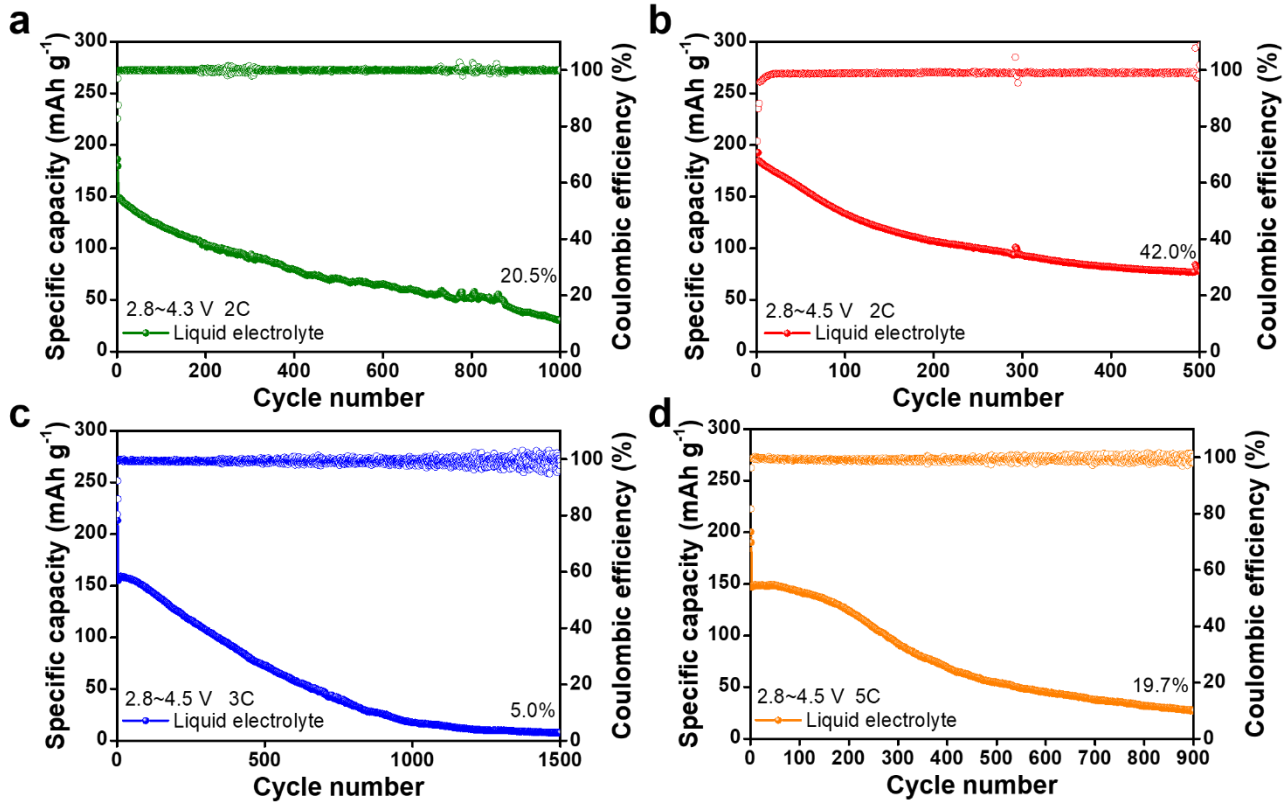

286

287 **Supplementary Figure 33 | Cycling stability of Li||NCM811 full cells using 1 M $LiPF_6$ in**

288 **EC/DMC/EMC (1:1:1) organic electrolyte.**

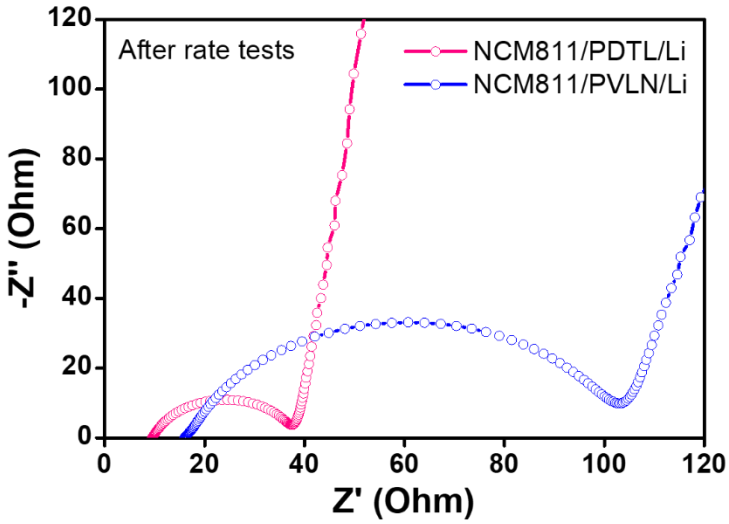

289

290 **Supplementary Figure 34 | EIS of Li||PVLN||NCM811 and Li||PDTL||NCM811 full cells after**

291 **rate tests.**

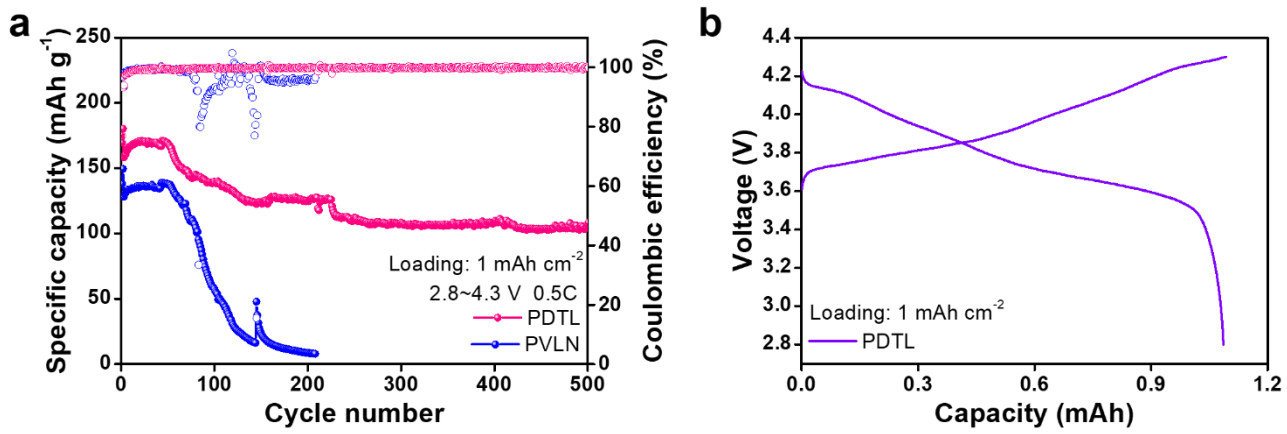

292

293 **Supplementary Figure 35 | Electrochemical performance of Li||NCM811 full cells at 2.8~4.3 V**

294 **with 1 mAh cm^{-2}.** a, cycling stability. b, Charge/discharge curves.

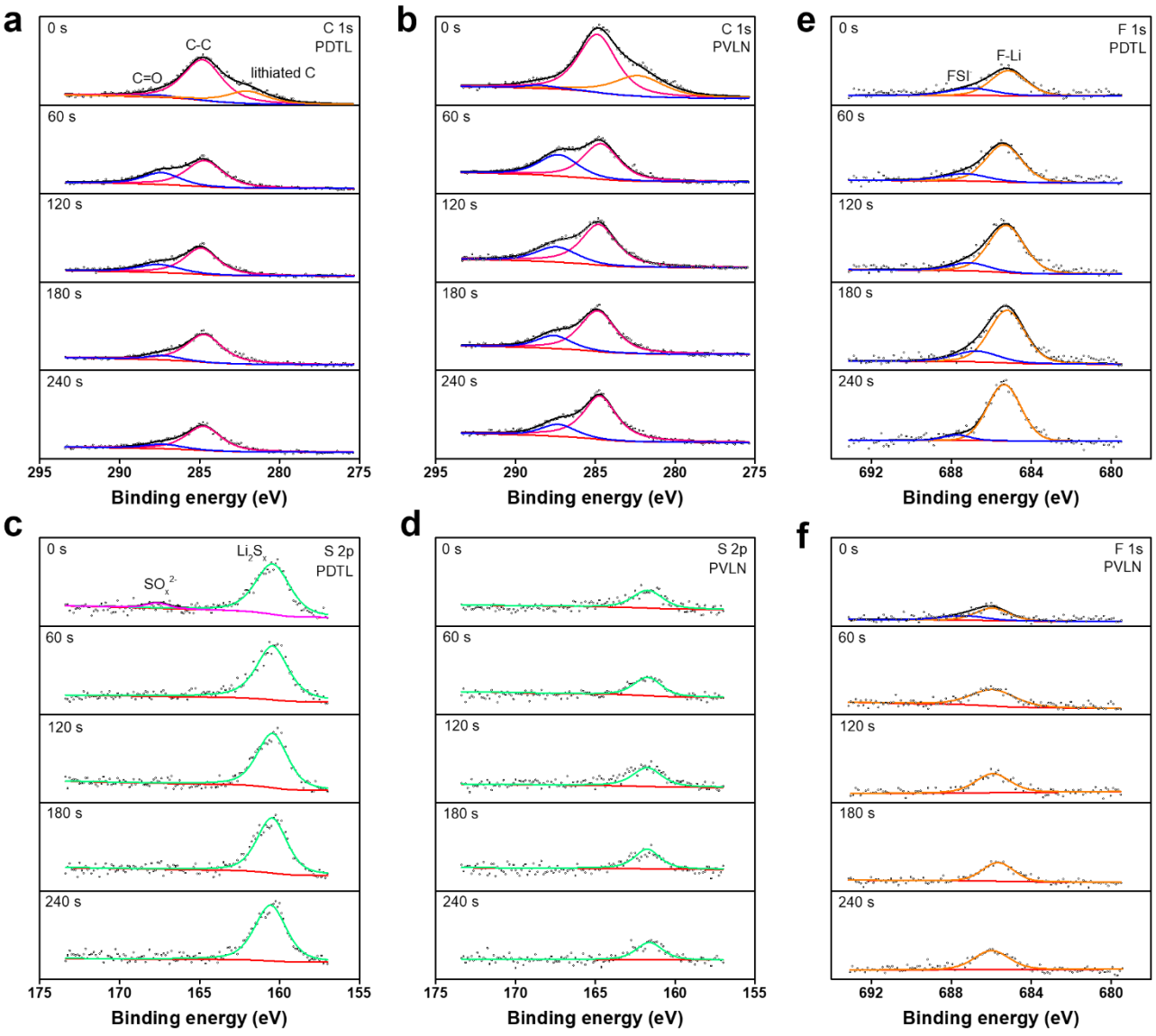

Supplementary Figure 36 | XPS spectra of cycled Li metal using PVLN and PDTL electrolyte.

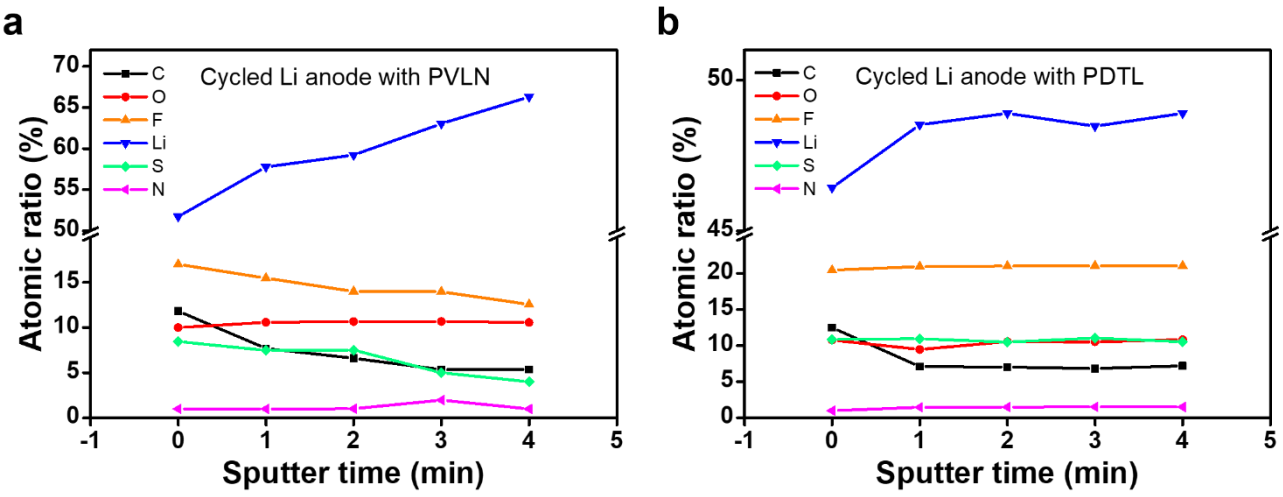

297

298 **Supplementary Figure 37 | Interfacial component analysis of cycled Li metal by XPS.** Quantified

299 interface atomic composition ratios of cycled Li metal using PVLN (a) and PDTL (b) electrolyte.

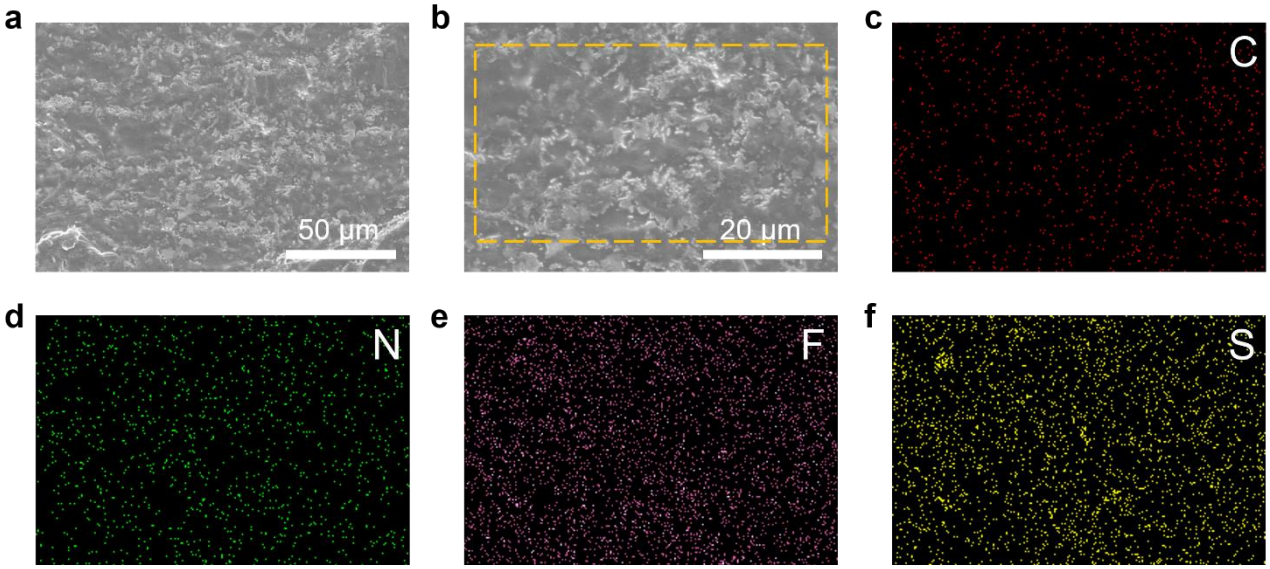

Supplementary Figure 38 | Surface SEM images of cycled Li metal using PVLN electrolyte and EDS element mappings.

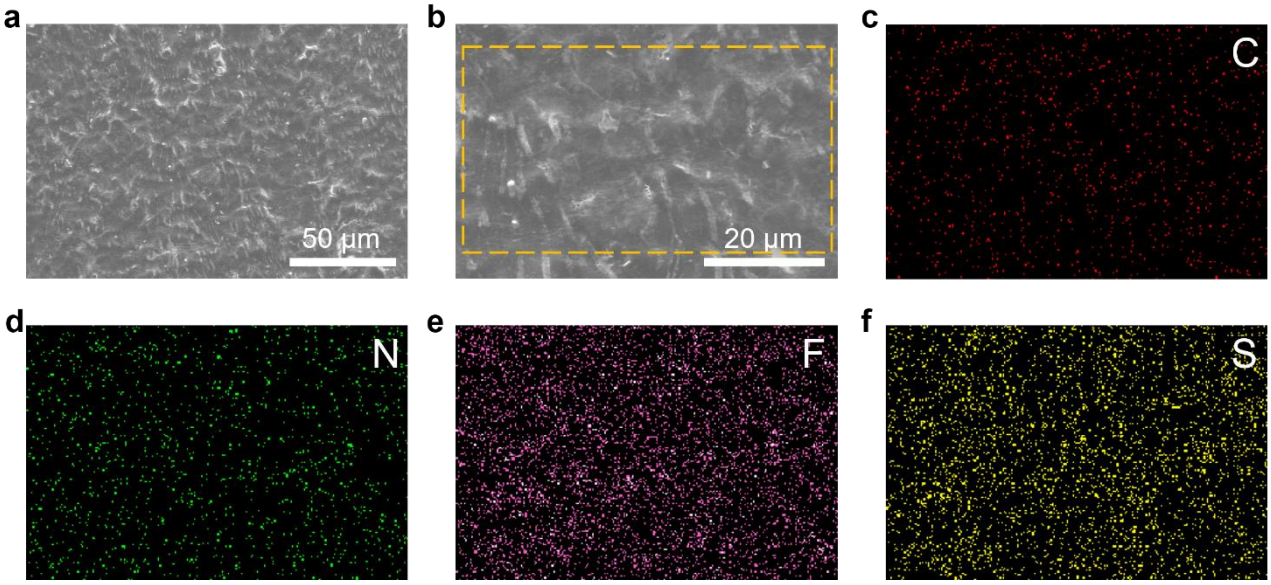

303

304 **Supplementary Figure 39 | Surface SEM images of cycled Li metal using PDTL electrolyte and**

305 **EDS element mappings.**

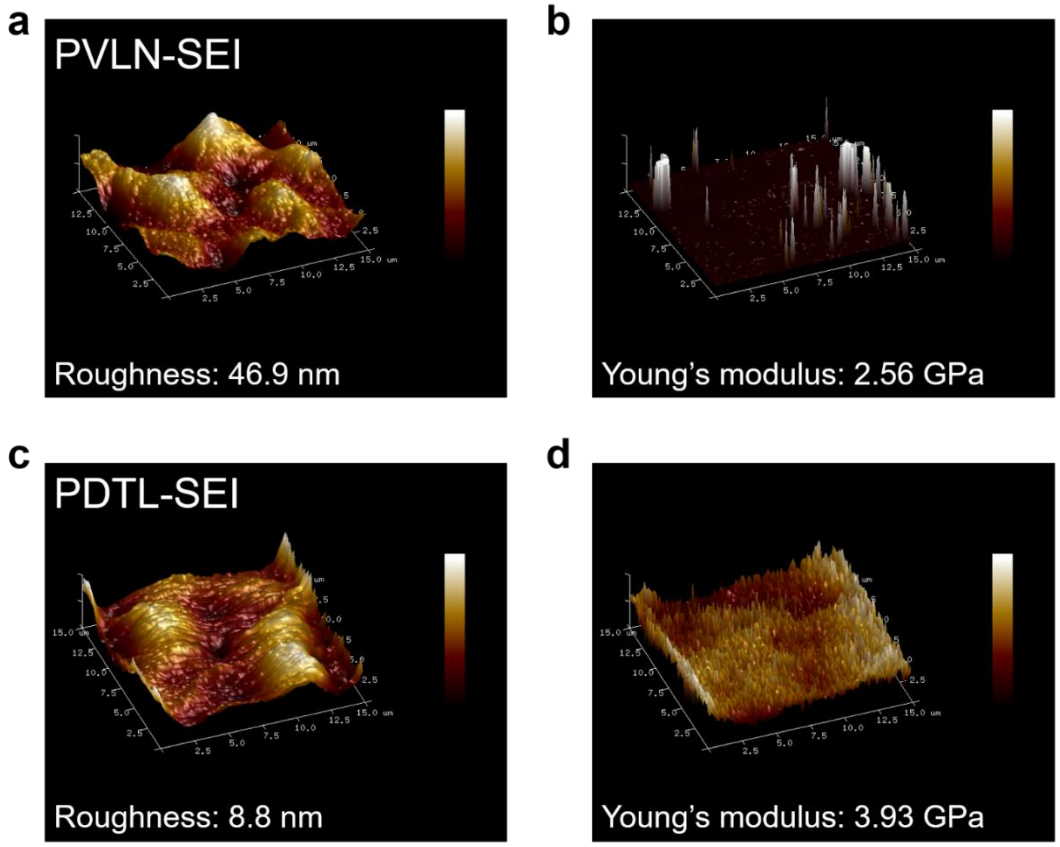

306

307 **Supplementary Figure 40 | AFM characterizations of cycled Li metal.** 3D AFM images of cycled
308 Li metal for roughness tests using PVLN (a) and PDTL (c) electrolyte. 3D AFM images of cycled Li
309 metal for Young's modulus tests using PVLN (b) and PDTL (d) electrolyte.

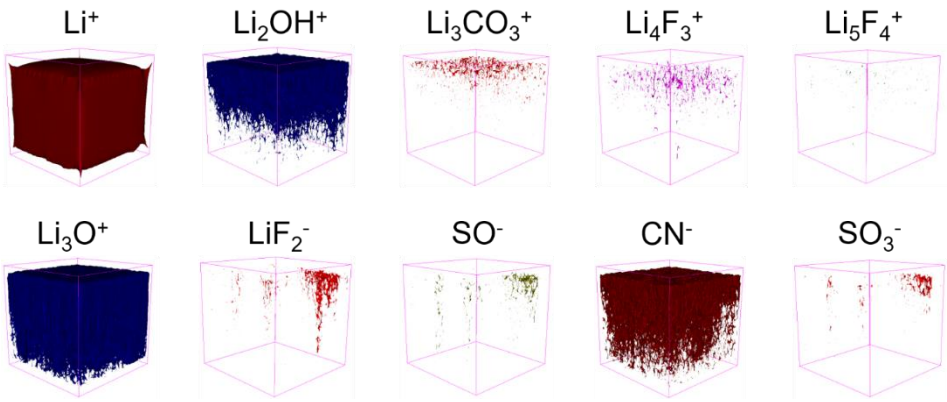

310

311 **Supplementary Figure 41 | TOF-SIMS 3D reconstruction of the sputtered volume on the cycled**

312 **Li surface using PVLN electrolyte.**

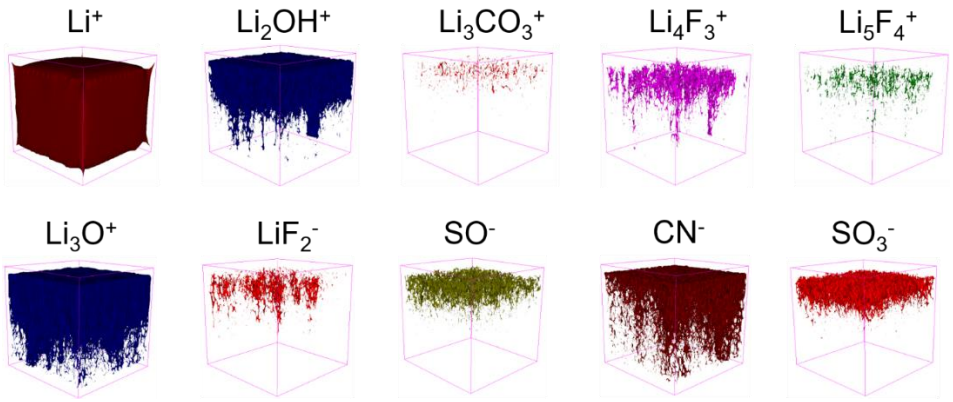

313

314 **Supplementary Figure 42 | TOF-SIMS 3D reconstruction of the sputtered volume on the cycled**

315 **Li surface using PDTL electrolyte.**

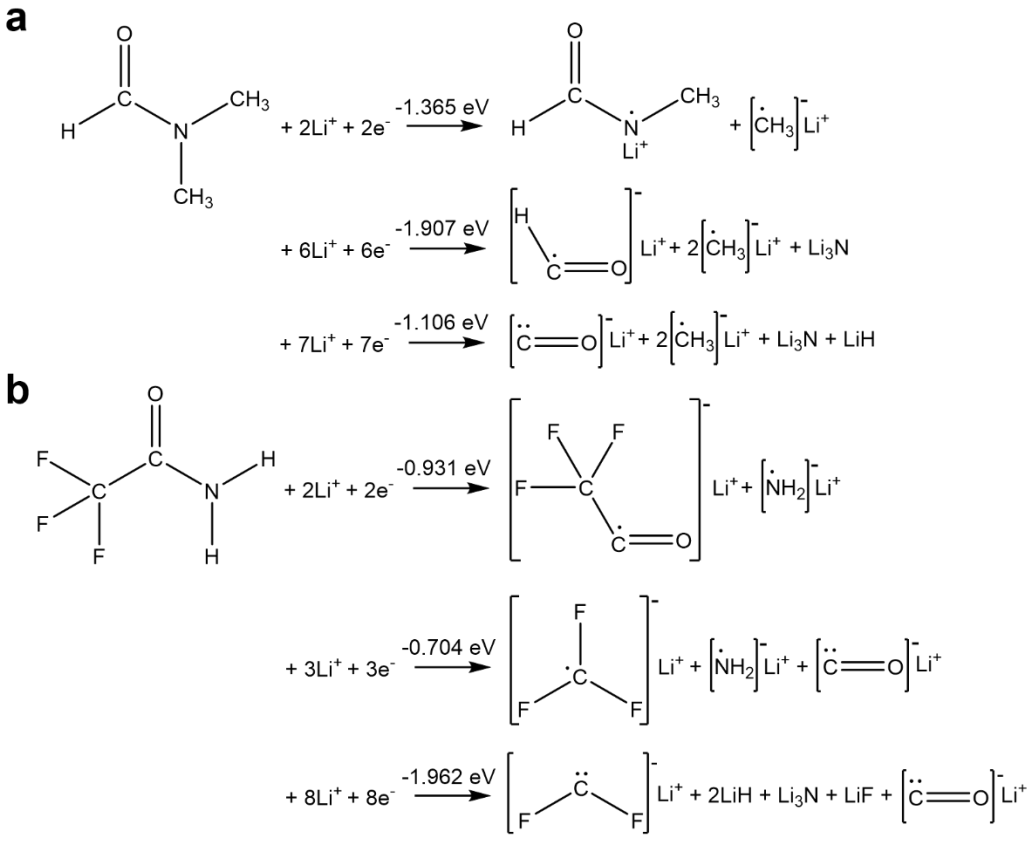

316

317 **Supplementary Figure 43 | Possible chemical reactions of solvent on Li metal.** Reduction reactions

318 of DMF (a) and TFA (b) on Li metal surface according to the reaction energy.

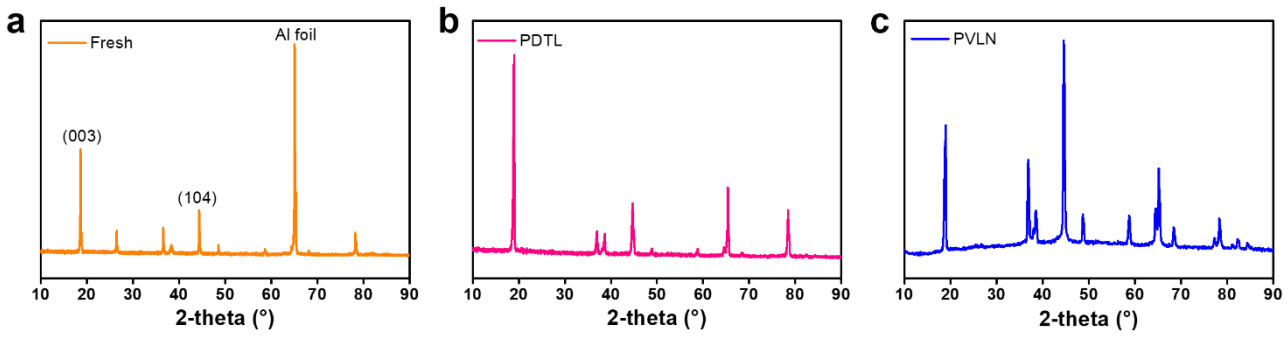

Supplementary Figure 44 | Structure characterizations of cycled NCM811. XRD patterns of pristine NCM811 (a), cycled NCM811 with PDTL (b) electrolyte and cycled NCM811 with PVLN (c) electrolyte.

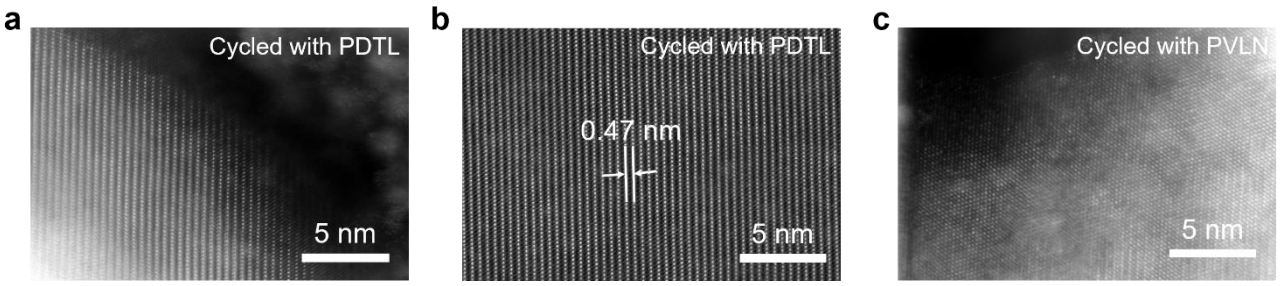

Supplementary Figure 45 | Nanostructures of cycled NCM811. HAADF-STEM images of cycled NCM811 with PDTL (a, b) and PVLN (c) electrolyte.

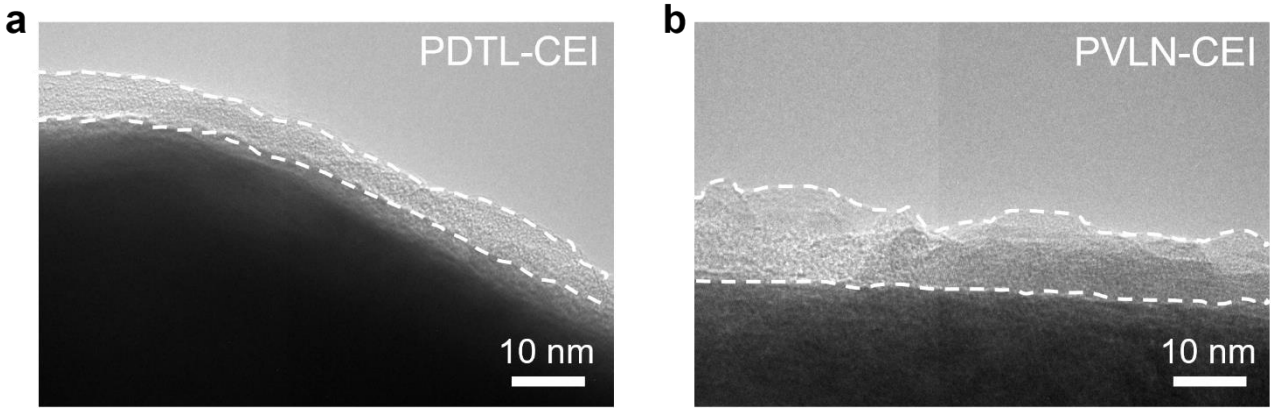

Supplementary Figure 46 | Surfaces of cycled NCM811. TEM images of the cycled NCM811 using PDTL (a) and PVLN (b) electrolyte.

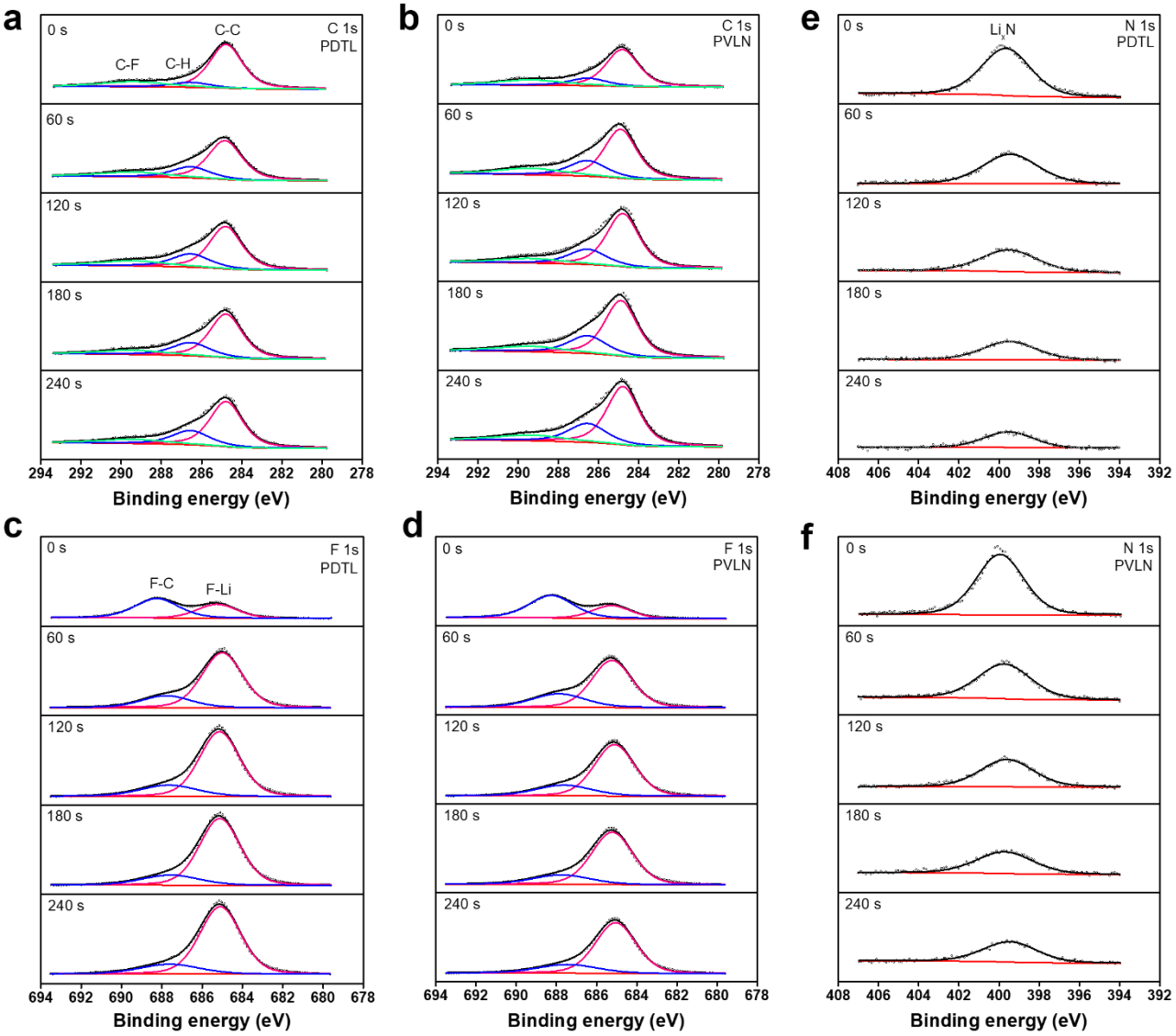

Supplementary Figure 47 | XPS spectra of cycled NCM811 using PVLN and PDTL electrolyte.

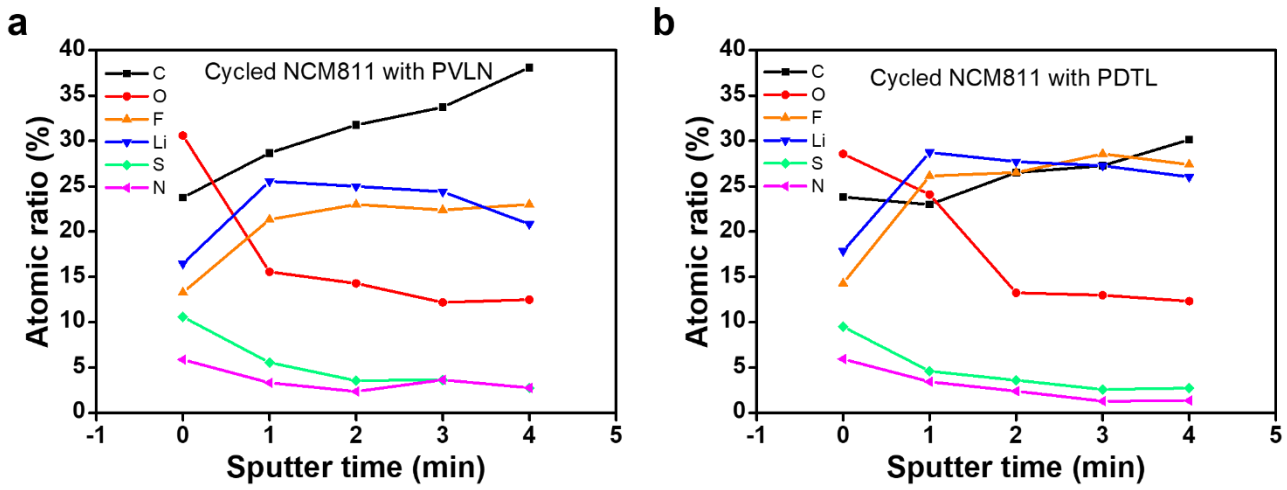

331

332 **Supplementary Figure 48 | Interfacial components analysis of cycled NCM811 by XPS.**
333 Quantified CEI atomic composition ratios of cycled NCM811 using PVLN (a) and PDTL (b)
334 electrolyte.

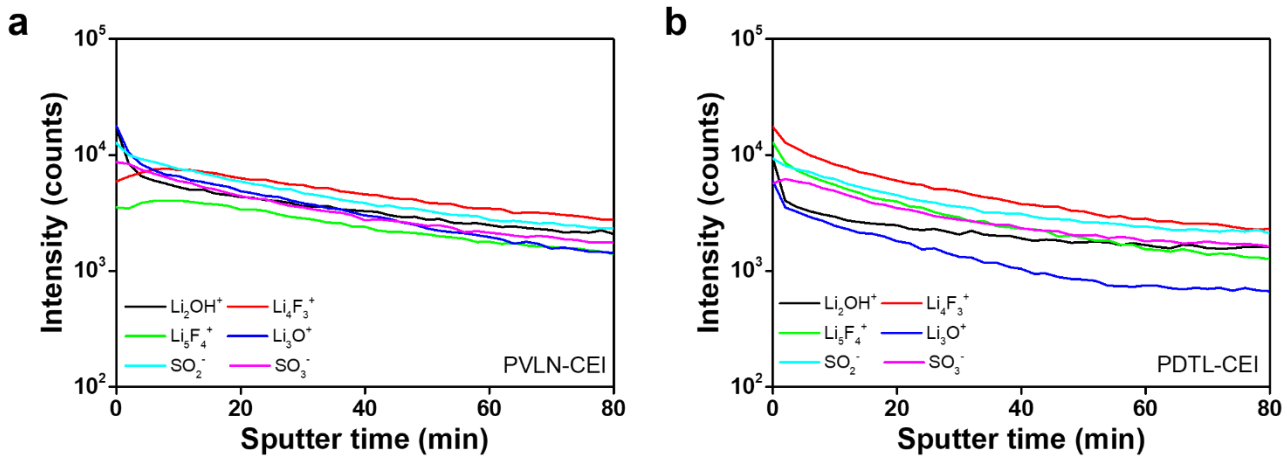

335

336 **Supplementary Figure 49 | TOF-SIMS depth profiling results of cycled NCM811.** TOF-SIMS
337 depth profiling of several secondary ion fragments on the cycled NCM811 using PVLN (a) and PDTL
338 (b) electrolyte.

Supplementary Tables

Supplementary Table 1 Comparation of Li||PDTL||Li symmetric battery performances.

Solid-state electrolyte	Li-Li symmetric battery performance	Reference
PVDF-$LiClO_4$/LLZTO particles	0.05 mA cm^{-2}-0.025 mAh cm^{-2} for 160 h	*J. Am. Chem. Soc.* **139**, 13779-13785 (2017)[12]
PVDF-LiFSI	0.1 mA cm^{-2}-0.1 mAh cm^{-2} for 2000 h	*Adv. Mater.* **31**, 1806082 (2019)[13]
PVDF-*b*-PTFE-LiTFSI/LLZAO/LLTO nanowires	0.2 mA cm^{-2}-0.2 mAh cm^{-2} for 1880 h	*Adv. Mater.* **33**, e2008084 (2021)[14]
PVDF-HFP/LiTFSI	0.3 mA cm^{-2}-0.15 mAh cm^{-2} for 300 h	*Angew. Chem. Int. Ed.* **60**, 12931-12940 (2021)[15]
PVDF/DEE	0.1 mA cm^{-2}-0.05 mAh cm^{-2} for 800 h	*Angew. Chem. Int. Ed.* **61**, e202205075 (2022)[16]
VEC/MASTFSILi/SN	0.1 mA cm^{-2}-0.1 mAh cm^{-2} for 1000 h	*Adv. Mater.* **34**, e2202143 (2022)[17]
PVDF-HFP/LiTFSI	0.1 mA cm^{-2}-0.1 mAh cm^{-2} for 4000 h	*Energy Environ. Sci.* **15**, 3379-3387 (2022)[18]
PEO/SN/FEC	1 mA cm^{-2}-1 mAh cm^{-2} for 400 h	*Nat. Nanotechnol.* **17**, 768-776 (2022)[19]
COF/LiTFSI/DMA	0.3 mA cm^{-2}-0.075 mAh cm^{-2} for 450 h	*Adv. Mater.* **34**, e2201410 (2022)[20]
P(VDF-TrFE-CTFE)/LiTFSI	0.05 mA cm^{-2}-0.05 mAh cm^{-2} for 1200 h	*Energy Environ. Sci.* **14**, 6021-6029 (2021)[21]
C_3mpyrFSI/LiFSI	0.2 mA cm^{-2}-0.2 mAh cm^{-2} for 2000 h	*Nat. Mater.* **20**, 1255-1263 (2021)[22]
$Al(Otf)_3$-LiTFSI/DOL	1 mA cm^{-2}-1 mAh cm^{-2} for 200 h	*Nat. Energy* **4**, 365-373 (2019)[23]
PVDF/LiFSI/LATP nanowires	0.5 mA cm^{-2}-0.5 mAh cm^{-2} for 700 h	*Angew. Chem. Int. Ed.* **60**, 24668-24675 (2021)[24]
PEGDA/UpyMA/LiTFSI/NML	0.2 mA cm^{-2}-0.2 mAh cm^{-2} for 2250 h	*Energy Environ. Sci.* (2022)[25]
PDTL	**0.5 mA cm^{-2}-0.25 mAh cm^{-2} for 2890 h 1 mA cm^{-2}-1 mAh cm^{-2} for 600 h**	**This work**

Supplementary References

1 Wang, Y. L., Shah, F. U., Glavatskih, S., Antzutkin, O. N. & Laaksonen, A. Atomistic insight into orthoborate-based ionic liquids: force field development and evaluation. *J. Phys. Chem. B* **118**, 8711-8723 (2014).

2 Abraham, M. J. *et al.* GROMACS: High performance molecular simulations through multi-level parallelism from laptops to supercomputers. *SoftwareX* **1-2**, 19-25 (2015).

3 Kuhne, T. D. *et al.* CP2K: An electronic structure and molecular dynamics software package - Quickstep: Efficient and accurate electronic structure calculations. *J. Chem. Phys.* **152**, 194103 (2020).

4 Hutter, J., Iannuzzi, M., Schiffmann, F. & VandeVondele, J. cp2k: atomistic simulations of condensed matter systems. *WIREs. Comput. Mol. Sci.* **4**, 15-25 (2014).

5 VandeVondele, J. & Hutter, J. Gaussian basis sets for accurate calculations on molecular systems in gas and condensed phases. *J. Chem. Phys.* **127**, 114105 (2007).

6 Krack, M. Pseudopotentials for H to Kr optimized for gradient-corrected exchange-correlation functionals. *Theor. Chem. Acc.* **114**, 145-152 (2005).

7 Becke, A. D. Density-functional exchange-energy approximation with correct asymptotic behavior. *Phys. Rev. A* **38**, 3098-3100 (1988).

8 Lee, C., Yang, W. & Parr, R. G. Development of the Colle-Salvetti correlation-energy formula into a functional of the electron density. *Phys. Rev. B* **37**, 785-789 (1988).

9 Kohn, W. & Sham, L. J. Self-Consistent Equations Including Exchange and Correlation Effects. *Phys. Rev.* **140**, A1133-A1138 (1965).

10 Blochl, P. E. Projector augmented-wave method. *Phys. Rev. B* **50**, 17953-17979 (1994).

11 Perdew, J. P., Burke, K. & Ernzerhof, M. Generalized Gradient Approximation Made Simple. *Phys. Rev. Lett.* **77**, 3865-3868 (1996).

12 Zhang, X. *et al.* Synergistic Coupling between $Li_{6.75}La_3Zr_{1.75}Ta_{0.25}O_{12}$ and Poly(vinylidene fluoride) Induces High Ionic Conductivity, Mechanical Strength, and Thermal Stability of Solid Composite Electrolytes. *J. Am. Chem. Soc.* **139**, 13779-13785 (2017).

13 Zhang, X. *et al.* Self-Suppression of Lithium Dendrite in All-Solid-State Lithium Metal Batteries with Poly(vinylidene difluoride)-Based Solid Electrolytes. *Adv. Mater.* **31**, 1806082 (2019).

14 Liu, S. *et al.* Solid-State Lithium Metal Batteries with Extended Cycling Enabled by Dynamic Adaptive Solid-State Interfaces. *Adv. Mater.* **33**, e2008084 (2021).

15 Liu, W. *et al.* Designing Polymer-in-Salt Electrolyte and Fully Infiltrated 3D Electrode for Integrated Solid-State Lithium Batteries. *Angew. Chem. Int. Ed.* **60**, 12931-12940 (2021).

16 Pei, X. *et al.* Li-N Interaction Induced Deep Eutectic Gel Polymer Electrolyte for High Performance Lithium-Metal Batteries. *Angew. Chem. Int. Ed.* **61**, e202205075 (2022).

17 Wen, K. *et al.* Ion-Dipole Interaction Regulation Enables High-Performance Single-Ion Polymer Conductors for Solid-State Batteries. *Adv. Mater.* **34**, e2202143 (2022).

18 Xu, S. *et al.* Decoupling of ion pairing and ion conduction in ultrahigh-concentration electrolytes enables wide-temperature solid-state batteries. *Energy Environ. Sci.* **15**, 3379-3387 (2022).

19 Lin, R. *et al.* Characterization of the structure and chemistry of the solid-electrolyte interface by cryo-EM leads to high-performance solid-state Li-metal batteries. *Nat. Nanotechnol.* **17**, 768-776 (2022).

20 Guo, D. *et al.* Foldable Solid-State Batteries Enabled by Electrolyte Mediation in Covalent Organic

Frameworks. *Adv. Mater.* **34**, e2201410 (2022).

21 Huang, Y.-F. *et al.* A relaxor ferroelectric polymer with an ultrahigh dielectric constant largely promotes the dissociation of lithium salts to achieve high ionic conductivity. *Energy Environ. Sci.* **14**, 6021-6029 (2021).

22 Wang, Y. *et al.* Solid-state rigid-rod polymer composite electrolytes with nanocrystalline lithium ion pathways. *Nat. Mater.* **20**, 1255-1263 (2021).

23 Zhao, Q., Liu, X., Stalin, S., Khan, K. & Archer, L. A. Solid-state polymer electrolytes with in-built fast interfacial transport for secondary lithium batteries. *Nat. Energy* **4**, 365-373 (2019).

24 Yang, K. *et al.* Stable Interface Chemistry and Multiple Ion Transport of Composite Electrolyte Contribute to Ultra-long Cycling Solid-State $LiNi_{0.8}Co_{0.1}Mn_{0.1}O_2$/Lithium Metal Batteries. *Angew. Chem. Int. Ed.* **60**, 24668-24675 (2021).

25 Wang, H. *et al.* A strongly complexed solid polymer electrolyte enables a stable solid state high-voltage lithium metal battery. *Energy Environ. Sci.* https://doi.org/10.1039/D2EE02904A (2022).